Effects of plan dimensions on gust wind loads for high-rise buildings

Liu, Y.; Kopp, Gregory; Chen, S.-F.

DOI:
10.1016/j.jweia.2019.103980

Document Version
Peer reviewed version

Citation for published version (Harvard):
Liu, Y, Kopp, G & Chen, S-F 2019, 'Effects of plan dimensions on gust wind loads for high-rise buildings', *Journal of Wind Engineering and Industrial Aerodynamics*, vol. 194, 103980.
https://doi.org/10.1016/j.jweia.2019.103980

Effects of plan dimensions on gust wind loads for high-rise buildings

Yi Liu[a], Gregory A. Kopp[b,*], Shui-fu Chen[a]

a. Institute of Structural Engineering, Zhejiang University, Hangzhou 310058, China

b. Boundary Layer Wind Tunnel Laboratory, Faculty of Engineering, University of Western Ontario, London, ON, Canada N6A 5B9

Abstract

Scale-model wind tunnel pressure measurements were carried out for rectangular-plan high-rise buildings with plan ratios ranging from 0.11 to 9. Mean, fluctuating, and peak wall pressure coefficient distributions and area-averages were investigated. In addition, comparisons with the ASCE 7-16 provisions for the Main Wind Force-Resisting System (MWFRS) were made. The results show that the plan ratio has significant effects on pressure coefficients on the leeward and side walls for plan ratios less than about 4. The largest mean base shear coefficient occurs for plan ratio of about 0.67, with large values in the range of 0.5 to 1, but decreasing for larger or smaller plan ratios. ASCE 7-16 mean load coefficients tend to underestimate the data, particularly because of the values on leeward walls. ASCE 7-16 also underestimates the peak load coefficients due to the value of the gust effect factor. For rigid buildings, ASCE 7-16 has a gust effect factor of 0.85, while measurements indicate that it is closer to 1 for plan ratios between 0.67 and 2. Thus, the overall mismatch between the ASCE 7-16 MWFRS loads and the measured data is due to both the mean pressure coefficients and the gust effect factor. For plan ratios below 0.67, the decrease in plan ratio tends to be favorable for the MWFRS load coefficients; while for plan ratios above 4, the effects of plan ratios on the MWFRS load coefficients are limited.

Keywords: wind loads; building aerodynamics; high-rise buildings; structural loads; wall pressure coefficients.

1 Introduction

The number of high-rise buildings has increased substantially over the past 5 decades. Traditionally, high-rise buildings served as commercial office buildings, but residential usage is also gaining popularity (Ali & Moon, 2007). For better natural ventilation and lighting effects, high-rise residential buildings are often designed with slab-type shapes, i.e., rectangular sections of large plan aspect ratios. For example, in a typical high-rise residential area shown in Fig. 1, the buildings are often about 100 m in height, 10 m to 15 m in width and 20 m to more than 90 m in length, leading to a large range of plan aspect ratios. For this kind of building, wind loads often govern the structural design. Even though there may be joints that separate the structural system into several independent units, from both the architectural and bluff-body aerodynamics perspectives, the wind loads should be determined based on the shape of the building and the appropriate plan aspect ratio.

Fig. 1 A typical slab-type high-rise residential area in China, where the buildings are usually assembled by 1 to 3 units, leading to plan aspect ratios ranging from 2 up to 8 or 9.

There have been many studies regarding wind loads on high-rise buildings, following the pioneering studies of Davenport and Cermak in the mid-1960s. Of particular interest here are the area-averaged pressure coefficients for the Main Wind Force-Resisting System (MWFRS). Among the many studies, the topic of effects of the building geometric parameters has been an important topic. For buildings with a rectangular plan, the height-to-width and the depth-to-breadth (i.e., plan) ratios, are important parameters. Fig. 2 defines the plan ratio, D/B, which is the focus of this study.

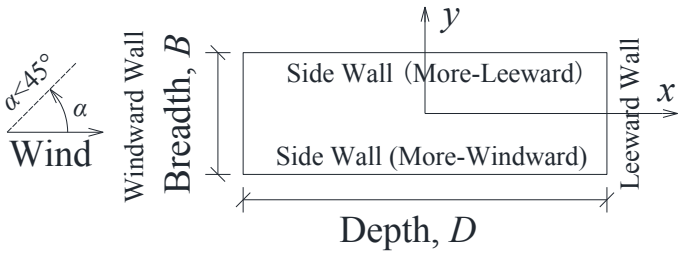

Fig. 2 Definition sketches of depth, *D*, and breadth, *B*. For the orthogonal wind direction, *D* and *B* are building plan dimensions that are parallel and normal to the wind, respectively; for oblique wind directions, *D* and *B* are defined with the same dimensions as for the orthogonal wind direction.

MWFRS pressure coefficients for rectangular high-rise buildings with different plan ratios have been reported by many previous studies. Miyoshi et al. (1971) measured mean pressure coefficients in wind tunnels for a building with plan ratio of 3.2. Dalgliesh (1975), Ohkuma et al. (1991) took full-scale measurements for tall buildings with plan ratios of 1.94 and 1.34, respectively. Cheung (1984), Kareem and Cermak (1984), McClean and Sumner (2014) reported mean, fluctuating (i.e., rms, root-mean-square) and peak pressure distributions and base force coefficients for buildings with a square cross-section (i.e., with a plan ratio of 1). Surry and Djakovich (1995), Zhou et al. (2003), Kim and Kanda (2010), Tanaka et al. (2012) investigated the effects of plan sections on surface pressures and base shears for high-rise buildings with plan ratios near 1. These studies provided valuable references on MWFRS wind loads for high-rise buildings with different plan ratios, while the effects of the plan ratio were not systematically investigated.

There are also studies that focused on the effects of plan ratios. Akins et al. (1976, 1977, 1980) investigated mean and fluctuating pressure coefficients on buildings with ratios of 0.25 to 4. These authors found that positive pressures on the windward wall are not strongly dependent on the plan ratio, while pressures on the leeward wall are significantly affected. As well, the pressures on the longer sides are less negative due to the flow reattachment and a more complete pressure recovery. Lin et al. (2005) investigated overall mean and rms force coefficients on buildings with plan ratios of 0.33 to 3 and also found that the plan ratio greatly influences net wind loads. In particular, there is a critical ratio of $D/B = 0.63$ with certain turbulence levels where the mean and rms drag coefficients reach their maximum values, and then decrease for larger *D/B* ratios due to interactions between the shear layers and leeward edge with intermittent reattachment (as can also be seen in Nakamura and Hirata, 1989). Amin and Ahuja (2014) investigated mean pressure coefficient distributions on buildings with *D/B* ratios in the range of 0.25 to 4 and found that when the *D/B* ratio exceeds a value of about 3, complete steady reattachment takes place on the side walls and the pressure coefficients on leeward walls become almost constant. As can be seen from the review above, most of the previous studies only focused on wind loads on buildings with plan ratios between 0.25 and 4.

However, as mentioned at the beginning, buildings with plan ratios beyond this range are fairly common today in many parts of the world.

For codes and standards, ASCE 7-16 (2016) gives external wall pressure coefficients for the MWFRS of buildings with different plan ratios. However, a detailed look at earlier versions, such as ASCE 7-93 (1993), indicates that, in the development of the ASCE 7 standard, the values of MWFRS pressure coefficients are partially based on AS1170.2-1973 (1973), with confirmation by wind tunnel tests and studies from Colorado State University during 1974 ~ 1978, including the studies of Akins et al. (1976, 1977, 1980) discussed above. These studies did not include discussions on buildings with plan ratios beyond the range of 0.25 to 4. This means that, although ASCE 7-16 provides suggested MWFRS pressure coefficients for such buildings, the experimental basis and the accuracy of the data for such buildings may not be adequate. In addition, ASCE 7-16 uses the gust effect factor to calculate the peak wind loads on MWFRS. The derivation of the gust effect factor (Solari, 1993a, 1993b; Solari and Kareem, 1998) for rigid buildings is based on many theoretical and parametric assumptions rather than direct measurements. Thus, it is also of practical importance to investigate peak MWFRS wind loads with the focus on the gust effect factor for rigid buildings.

To this end, the boundary layer simulation in wind tunnel experiments also plays a significant role in determining the resulting wind loads. It is now well known that, not only a correct simulation of the mean velocity profile, but also accurate simulations of the turbulence intensities and spectra, are required. However, even though some studies discussed above have similar power law velocity profiles, the turbulence intensity profiles show large differences. This may lead to differences in peak pressure coefficients for MWFRS (as well as Components and Cladding) because of changes to both the intensity and extent of separated flow regions (Bearman and Morel, 1983; Lander et al., 2016; Akon and Kopp, 2016). As mentioned above, the wind tunnel tests for the current ASCE 7 provisions were conducted more than 40 years ago, and these particular provisions (i.e., the pressure coefficients) have not been updated for decades even though there have been many advances in wind tunnel facilities, data processing techniques, and changes in wind simulation approaches. Given recent changes to other pressure coefficients in ASCE 7-16, e.g., Kopp and Morrison (2018), it is of interest to re-visit these coefficients as well.

Thus, the objective of this study is to systematically examine the effects of plan dimensions on mean and peak wind loads acting on rigid rectangular high-rise buildings, with an additional focus on the comparison with ASCE 7-16 provisions. In order to achieve this objective, wind tunnel pressure tests were conducted for rectangular-plan high-rise building models with 21 different plan ratios ranging from 0.11 to 9. Mean, rms, and peak pressure coefficient distributions, MWFRS area-averages for the wall loads and the gust effect factors are analyzed in detail, together with comparisons to the ASCE 7-16 provisions.

2 Experimental Set-Up

2.1 Wind simulation

The experiments were carried out in the high-speed test section of the closed-return Boundary Layer Wind Tunnel Ⅱ at the University of Western Ontario (UWO). The high-speed test section is 3.4 m (11 ft) wide, 2.1 m (7 ft) high, 30 m (100 ft) long from inlet to the center of the turntable, with a maximum wind speed of 30 m/s. The wind tunnel floor has fully automated surface roughness elements, with blocks that have a maximum height of 200 mm (8 in), to generate the desired boundary layer characteristics. At the inlet of the test section, turbulence generating devices, including sawtooth trips, spires, and barriers can also be added. For the present experiments, all of these were used to develop an upstream condition simulating an open exposure. Wind speeds were measured by using a Cobra Probe (TFI, Model no. 900) at a sampling frequency of 1250 Hz (Akon, 2017), with a reference wind speed of 10.4 m/s at 1.47 m (58 in) above the wind tunnel floor. The length scale of the wind field was found to be 1:200 (Hong, 2017). Fig. 3 shows the fit between the measured profiles and the target open terrain profiles, where $\overline{U}_z$ and I_{uz} are the mean wind velocity and turbulence intensity at height, z, respectively. The profiles in Fig. 3 are based on the log law, as applied by ESDU (1982, 1985), and have been referenced to the building roof height, H. The measured velocity profile is slightly fuller than both the log law and power law fits for z/H < ~0.6, while there is an excellent match for z/H > 0.6.

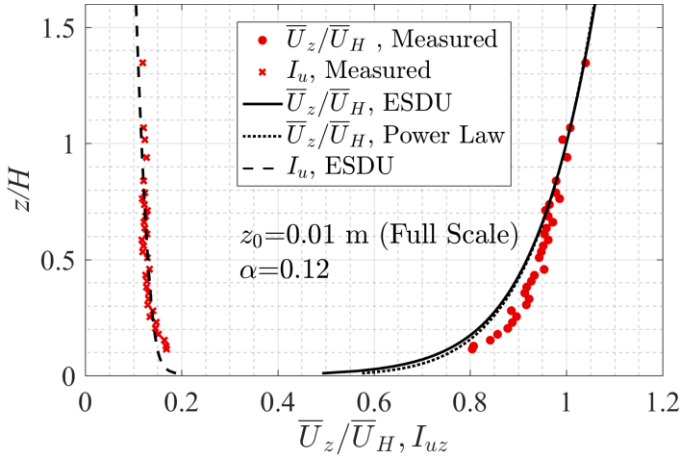

Fig. 3. Normalized mean velocity and turbulence intensity profiles.

For the turbulence intensity profile, the equations in ESDU 85020 (1985) are used to obtain the target profile. A value of 0.01 m is found for the aerodynamic roughness, z_0, which is obtained by matching both the mean velocity profile and turbulence intensity profile. This is within the range of expected values for open terrain exposures and yields an excellent fit with the measured data.

Fig. 4 shows the measured integral length scale profile and several models for it including

ESDU 74 (1974), ESDU 85 (1985), Solari (1993a) and Tieleman (2003). For the measured data, the integral length scale, L_u, can be obtained by:

$$L_u = \bar{U}_z L_t, \quad L_t = \int_0^{\tau_0} \rho_{uu}(\tau)\ \mathrm{d}\tau \tag{1}$$

where L_t is the integral time scale and is obtained by integrating the autocorrelation of wind speed time series, $\rho_{uu}(\tau)$, from 0 to τ_0, the time lag where $\rho_{uu}(\tau)$ first reaches zero. There is scatter in the measured profile which is likely due to a relatively short duration of wind tunnel sampling time for this statistic. However, the scatter in the measurements is relatively small compared to the variation in the models that could be used as target values for the experiments. It is noted that ESDU 74 is typically used in experiments conducted at UWO (e.g., Ho et al., 2005), and that Solari (1993a) is used in the gust effect factor analysis which is the basis for ASCE 7-16 MWFRS loads. Overall, the measured values tend to be bound by the ESDU 74 and Solari models, indicating that the current scales are reasonable for the current terrain simulation.

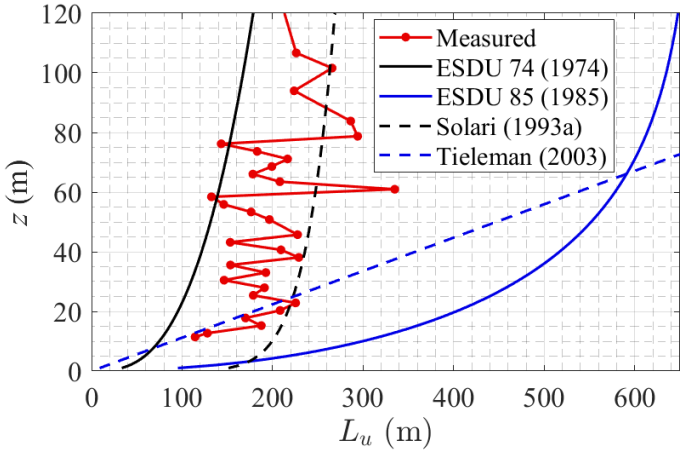

Fig. 4 Integral length scale profile in full scale

Fig. 5 shows the fit between the measured streamwise velocity spectrum and the von Karman spectrum at an equivalent full-scale height, z = 76.2 m (z/H = 0.762, which is close to the height of the stagnation point on the building models considered below). The von Karman spectrum is given by:

$$\frac{f S_{uu}(n)}{{\sigma_u}^2} = \frac{4 f_u}{\left(1 + 70.8 {f_u}^2\right)^{\frac{5}{6}}}, \quad f_u = \frac{f L_u}{\bar{U}_z} \tag{2}$$

for the velocity fluctuations in the along-wind direction (ESDU, 1974), where f is the frequency, $S_{uu}(n)$ is the power spectral density. From Fig. 5, one can see that there is, overall, a good agreement between the measured and target velocity spectra, noting, once again, that there is uncertainty in the target integral scales which would alter the match at other heights.

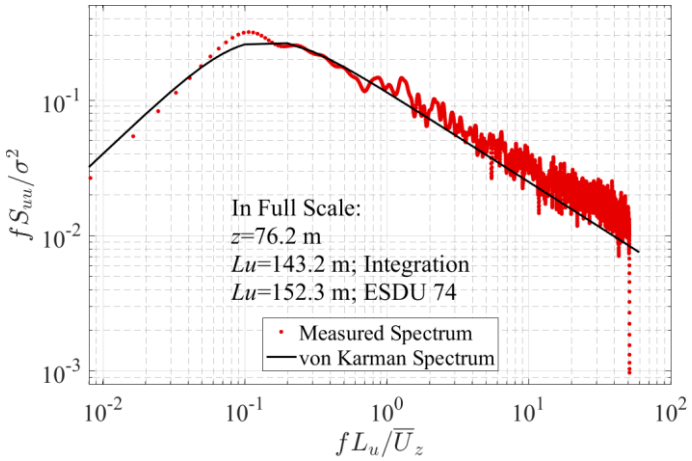

Fig. 5. Velocity spectra for u components at an equivalent full-scale height, z = 76.2 m (z/H = 0.762).

2.2 Building models and Pressure tests

The models for the pressure tests were made by University Machine Services at the University of Western Ontario. The length scale of the models is 1/200, equal to the length scale of the wind field. The dimensions of the model and corresponding dimensions of the building in full scale are listed in Table 1. The model is constructed with 12 removable sections, which are labeled as S1 to S12, as shown in Fig. 6. Adjacent sections are connected and fastened by screws, so the assembled model can be treated as rigid. When all 12 sections are assembled together, a plan ratio of D/B = 9 (or 1/9) is obtained. The configurations for different D/B ratios, from 0.11 to 9, are obtained by assembling different sections together. In total, 21 different plan ratios are used in this study, as listed in Table 2.

Table 1 Model details

	Height, H [m]	Width [m]	Length [m]	Plan ratio D/B	Length scale
Model scale	0.5	0.06	0.06 to 0.54	0.11 to 9	1/200
Full scale	100	12	12 to 108		

Fig. 6 and Fig. 7 provide the pressure tap layouts. Each segment has 7 levels of pressure taps, in the same layout in vertical direction, as shown in Fig. 6. The vertical locations are at 0.1H, 0.3H, 0.5H, 0.65H, 0.8H, 0.9H and 0.98H, respectively. For the configuration with D/B = 9, each vertical level has 88 pressure taps, for a total of 616 pressure taps. This number of taps is reduced for configurations with reduced D/B ratios (for $D/B \geq 1$), as listed in Table 2.

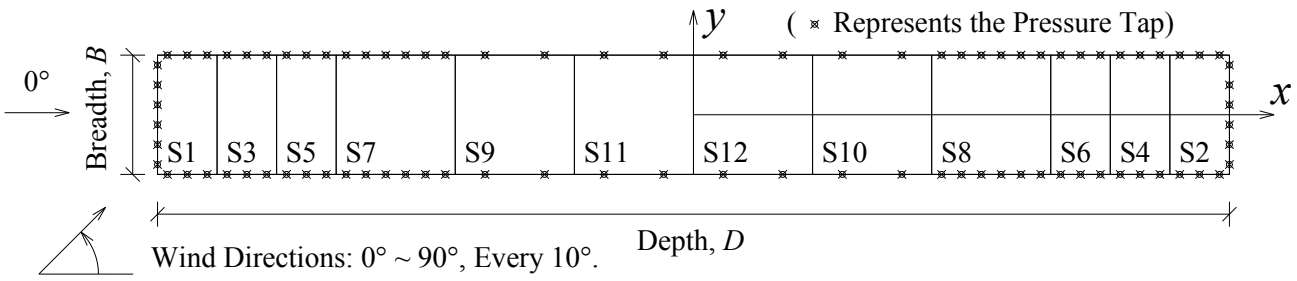

Fig. 6. Plan view of the model configuration for D/B = 9, including the definition of coordinate system, wind direction, and the layout of pressure taps on each section.

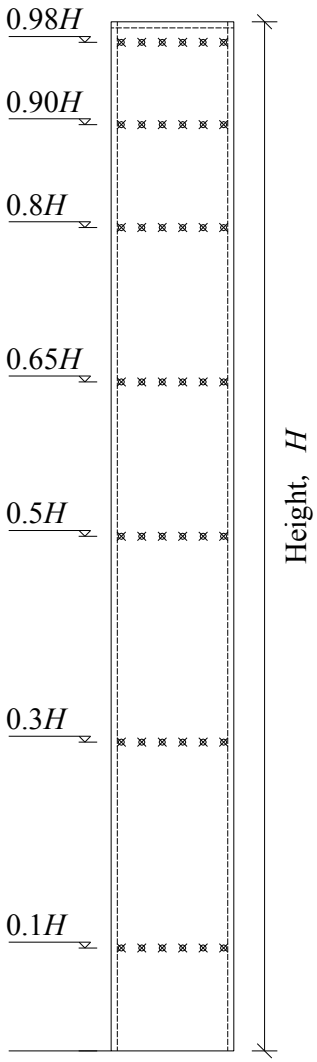

Fig. 7. Side view of the model and layout of pressure taps, which is the same for all configurations.

Table 2 Details for the different building configurations

Plan ratio *D/B*	Sections assembled	Number of Pressure Taps
1/9, 9	1,3,5,7,9,11,12,10,8,6,4,2	616
1/8, 8	1,3,5,7,9,11,10,8,6,4,2	588
1/7, 7	1,3,5,7,9,10,8,6,4,2	560
1/6, 6	1,3,5,7,10,8,6,4,2	532
1/5, 5	1,3,5,7,8,6,4,2	504
1/4, 4	1,3,5,7,6,4,2	420
1/3, 3	1,3,5,6,4,2	336
1/2.5, 2.5	1,3,5,4,2	294
1/2, 2	1,3,5,2	252
1/1.5, 1.5	1,4,2	210
1	1,2	168

The pressure taps were connected to pressure scanners, which have 16 ports each. The tubing system has a flat frequency response up to about 200 Hz, further details can be found in Ho et al. (2005). The pressure data were sampled at a frequency of 400 Hz, with a total sampling duration of 90 seconds, which is long enough to represent 1 hour in full scale using a velocity scale of 1/5, leading to a time scale of 1/40. In total, time series of 36,000 pressure coefficients per tap, for each wind direction and configuration, were obtained.

The blockage ratios for the tested configurations vary between 0.42% and 3.77%, which are lower than maximum allowable values in ASCE 49-12 (2012). No corrections for the blockage ratio were made. The measurements were made with a reference wind speed of 14.0 m/s at a height of 1.47 m (58 in) above the wind tunnel floor, in a region where the wind speed is uniform. The Reynolds number based on the wind speed at the roof height and building breadth, B, (for $D/B \geq 1$) was about 5.8×10^4. For each D/B configuration, 10 different wind directions from 0° ~ 90° in 10° increments were tested. (It should be noted that when the wind direction is larger than 45°, D and B reverse so that the ratio will transfer to its reciprocal, according to Fig. 2.) By symmetry, this captures the full range of wind directions. The wind directions and coordinates are defined in Fig. 6. The origin of the coordinate system always locates at the center of the model.

Following the usual convention in wind engineering, pressure coefficients are referenced to the dynamic pressure at the roof height, H, as denoted by:

$$C_p(t) = \frac{P(t) - P_\infty}{0.5\rho\bar{U}_H^{\,2}} \tag{3}$$

where $P(t)$ is the time-varying total wind pressure at a location on the building surface, P_∞ is the static pressure, and $\bar{U}_H$ is the mean wind speed at the roof height. Because the pressure coefficients are stochastic variables, the use of statistical values of $C_p(t)$ is important. The mean pressure coefficient is the time average of the $C_p(t)$, denoted as $\bar{C}_p$, while the rms (root-mean-square fluctuating, or standard deviation) pressure coefficient is denoted as C_p' (=σ_{Cp}).

In addition to the pressure coefficient defined above, "local" pressure coefficients are also defined, where the reference dynamic pressure is at the height of the tap and is denoted as:

$$C_{pL}(t) = \frac{P(t) - P_\infty}{0.5\rho\bar{U}_z{}^2} \tag{4}$$

where $0.5\rho\bar{U}_z{}^2$ is the mean dynamic pressure at height, z.

2.3 Comparisons with published data

Mean pressure coefficients were compared with previously published data in the literature to check the reliability of the current data. Due to the similar geometry with the CAARC standard tall building model, data from Melbourne (1980) are used here for the comparison. The CAARC model has a plan ratio of 0.67; for tests in this paper, data of the configuration with the same plan ratio are used for the comparison. It should be noted that, due to the differences in mean wind speed profiles, if mean pressure coefficients referenced to the mean dynamic pressure at the roof height (i.e., using $\bar{C}_p$), the comparisons will show significant differences. Therefore, all of the mean pressure coefficients are re-referenced to the dynamic pressure at the local elevation by using the velocity profiles presented in the references (i.e., $\bar{C}_{pL}$ are used). This reduces the effects of using different wind velocity profiles, making the results more comparable.

Fig. 8 shows the $\bar{C}_{pL}$ data found in the literature and from the current study. In addition, the power law exponent, α, and the turbulence intensity, I_u, at this height are given in the legend. As can be seen in Fig. 8, the data match reasonably well with the current data being within the spread of the published results. It can be observed that the range of variation is ±0.1 C_p, or ±10% for $C_p \approx 1.0$. Some of these variations may be attributed to uncertainty in the velocity profiles from the various studies and also to the difference in height-to-width ratio. In any case, this range is typical of measurement uncertainty on pressure coefficients (Diaz, 2006). In addition, differences may also be caused by variations in the turbulence intensities, which range from 11% to 13% at this height in the cited studies. In any case, the current data appear to be reasonable, in comparison with the previously published data.

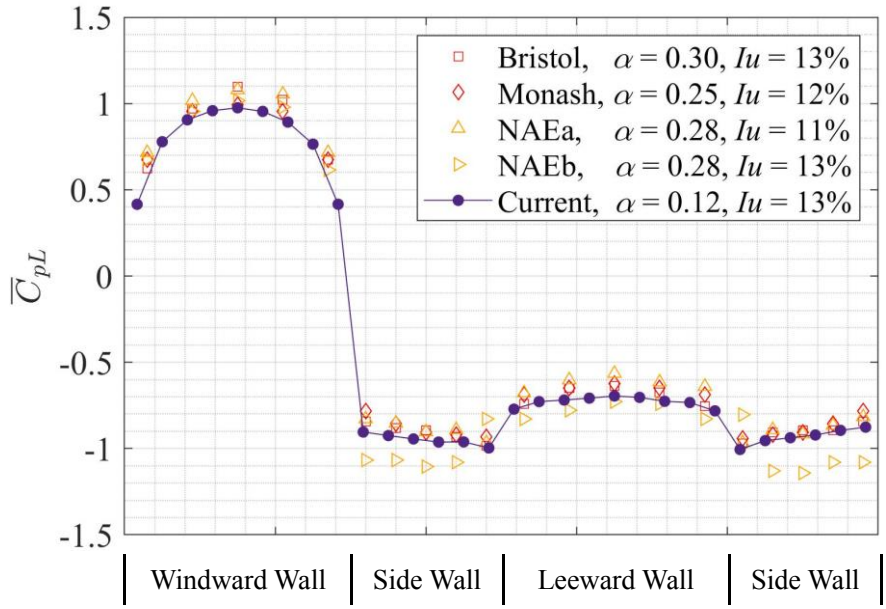

Fig. 8. Comparison between the mean local pressure coefficients, $z/H = 0.65$ for the current study and $z/H = 0.67$ for the referenced data, under the orthogonal wind direction.

3 Wall pressure coefficient distributions

In order to get an overall understanding of the spatial characteristics of $\bar{C}_p$ and C'_p, the distributions on the windward, leeward, and side walls under the orthogonal wind direction for the range of D/B ratios considered, are examined in this section. Fig. 9, Fig. 10 and Fig. 11 show the distributions of $\bar{C}_p$ and C'_p on the windward, leeward, and side walls, respectively. In these figures, each box represents the area of a pressure tap, while the color scale for the pressure coefficients is provided in the figure. In this paper, darker reds always indicate a larger positive pressure coefficient, while the darker blues indicate a more negative value. Fig. 12 provides vertical and horizontal line plots to allow for more systematic understanding of the pressure coefficient variations with geometry.

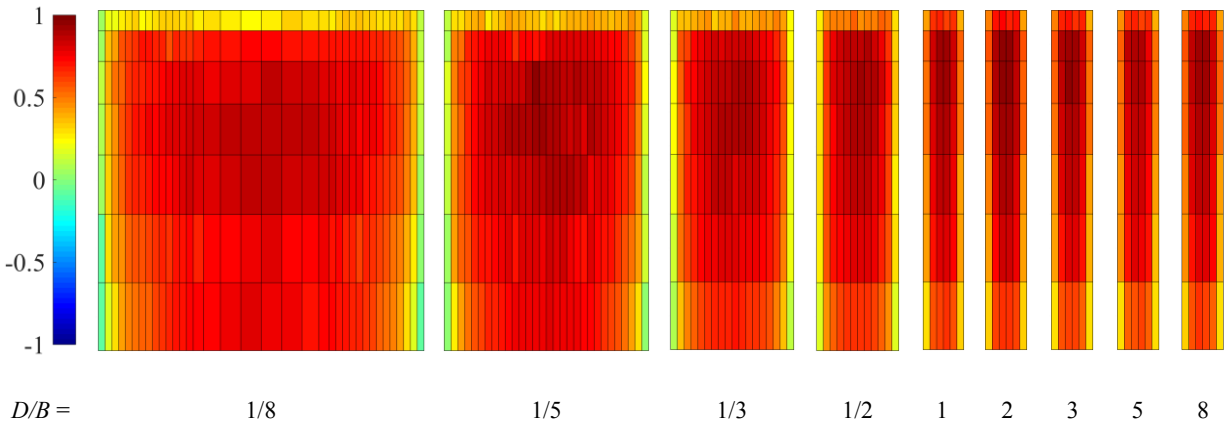

(a)

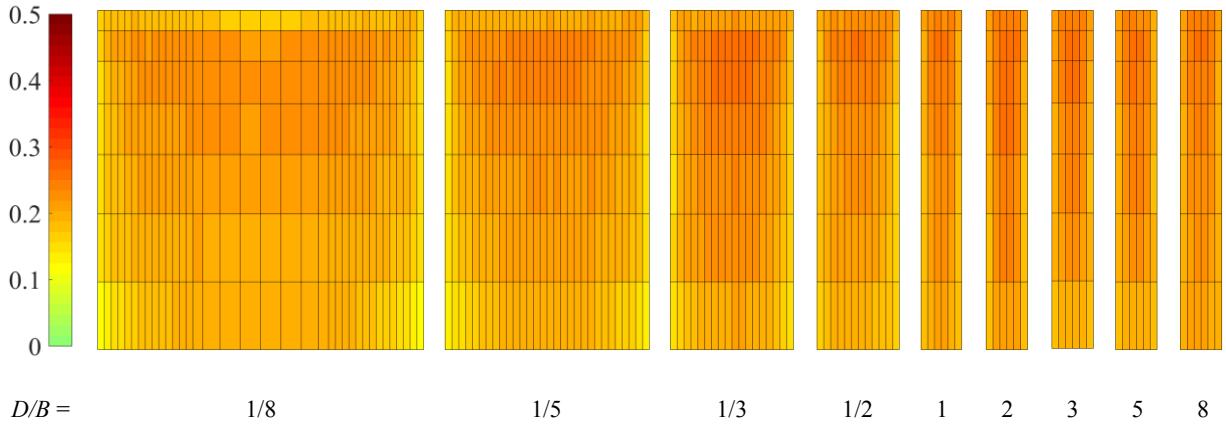

(b)

Fig. 9. Pressure coefficient distributions on the windward wall under the orthogonal wind direction for (a) $\bar{C}_p$ and (b) C'_p.

3.1 Windward wall

From Fig. 9(a) and Fig. 12(a) it can be seen that, on the windward wall, $\bar{C}_p$ distributions are similar for all *D/B* ratios. $\bar{C}_p$ reaches its maximum on the centerline of the windward wall at the stagnation point. Away from the stagnation point, the mean pressure is lower towards all of the edges. For $D/B \geq 1$, the stagnation point is located between about $z/H = 0.8$ and 0.9. For $D/B < 1$, the stagnation point is in a lower position, reducing from about $z/H = 0.8$ to 0.65 for lower *D/B* ratios. The pressure level is also reduced near the top (i.e., the roof edge) for $D/B < 1$, with more significant reductions for the lowest *D/B* ratios. In contrast, for $D/B \geq 1$, the $\bar{C}_p$ distributions are nearly the same for all configurations. The pressure fluctuation, C'_p, distributions on the windward wall have similar patterns as the $\bar{C}_p$ distributions, with maximum values located near $z/H = 0.9$ for $D/B \geq 1$, but at $z/H = 0.9$ to 0.8 for $D/B < 1$.

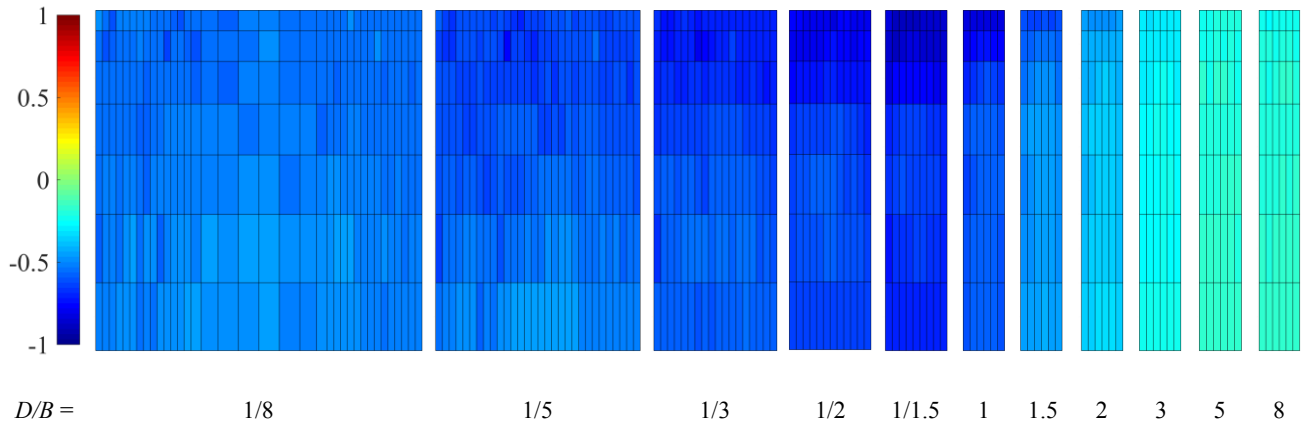

(a)

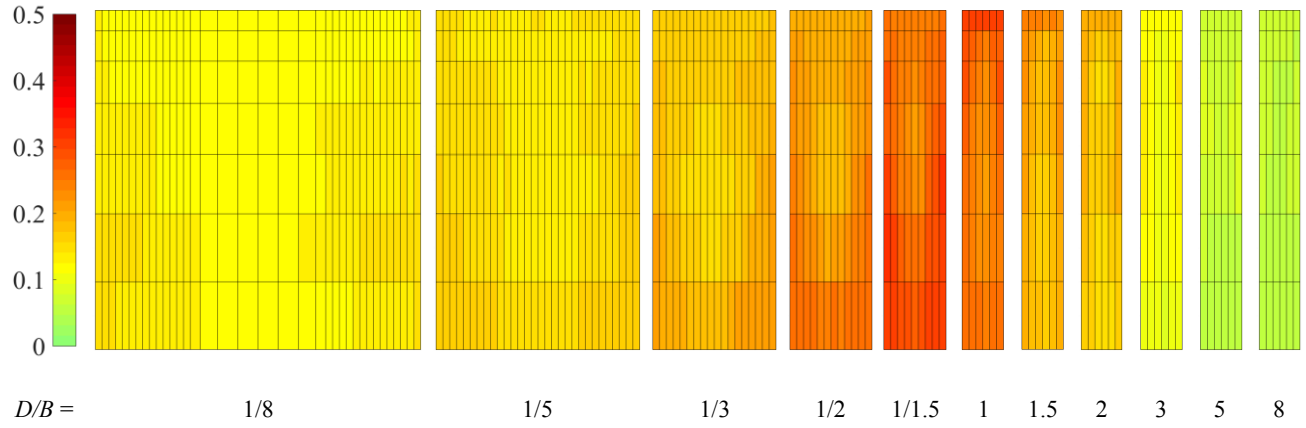

(b)

Fig. 10. Pressure coefficient distributions on the leeward wall under the orthogonal wind direction for (a) $\bar{C}_p$ and (b) C'_p.

3.2 Leeward wall

On the leeward wall, Fig. 10 and Fig. 12(b) indicate that the distributions of both $\bar{C}_p$ and C'_p are approximately uniform over the entire leeward wall for all *D/B* ratios, except for *D/B* = 0.5 to 1.5 where $\bar{C}_p$ is reduced (i.e., larger suctions) and C'_p is slightly larger in the regions near the top and side edges. However, large differences between the various *D/B* configurations can be observed. The largest suctions are observed for *D/B* = 0.5 to 1, where $\bar{C}_p$ reaches minimum values smaller than -0.7. For larger *D/B* ratios, $\bar{C}_p$ becomes less negative, with values of about -0.3 for *D/B* = 2.5 and -0.2 at *D/B* = 4. For $D/B \geq 4$ the mean coefficients are nearly constant. For the pressure fluctuations, the largest average C'_p values of about 0.3 occur at *D/B* = 1, but are smaller for all other *D/B* ratios decreasing to about 0.05 by *D/B* = 4 and to about 0.1 for *D/B* = 0.125.

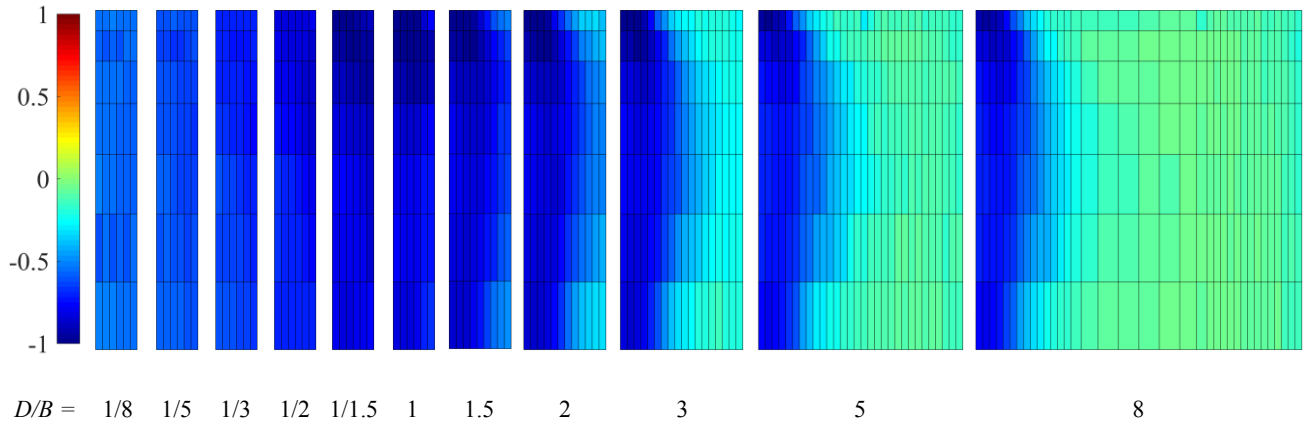

(a)

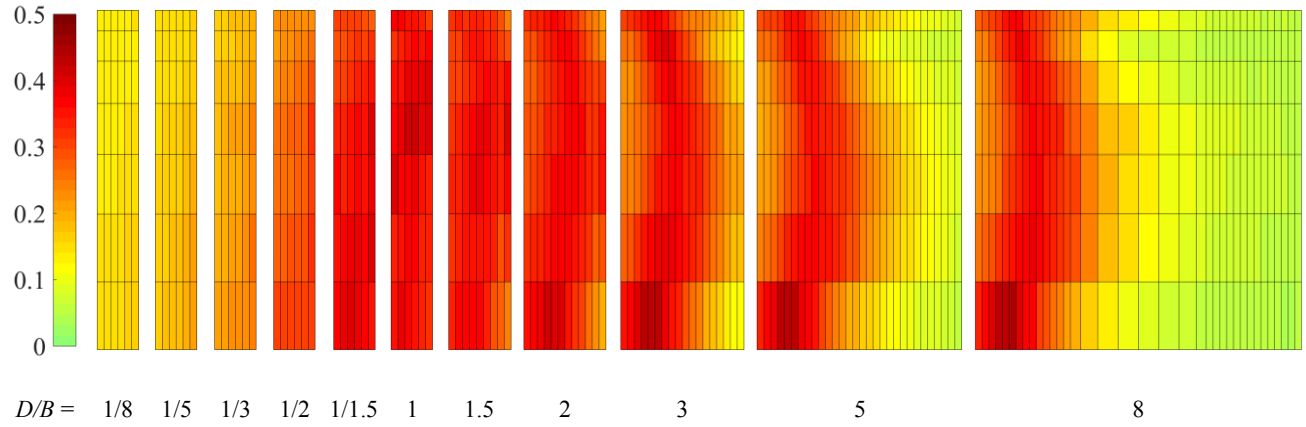

(b)

Fig. 11. Pressure coefficient distributions on the side walls under the orthogonal wind direction for (a) $\bar{C}_p$ and (b) C'_p. Wind direction: from left to right.

3.3 Side walls

On the side walls, there are large differences between different *D/B* ratios, as can be seen in Fig. 11 and Fig. 12(c). In Fig. 12(c), pressure coefficients are plotted against the distance from the leading edge, *d*, but which are normalized by *B* and *D* for $D/B \geq 1$ and $D/B \leq 1$, respectively, for better observations of the data patterns. Overall, the configurations with the largest suctions and pressure fluctuations are for *D/B* = 0.67 to 1.5. For other *D/B* ratios, the magnitudes of both the mean and fluctuating pressures tend to be reduced.

For $D/B > 1$, the $\bar{C}_p$ distributions near the leading edge are close to being self-similar, with a tendency to slightly larger suctions for smaller plan ratios. Akon and Kopp (2016) developed a model for estimating mean reattachment point locations from mean pressure distributions, based on pressure and velocity field measurements for low-rise building roofs and published results for two-dimensional rectangular prisms in uniform flow. Given the similar flow characteristics and

aerodynamic force distributions under separated and reattaching flows, Akon and Kopp's method is used here to estimate the mean reattachment lengths on the side walls. Akon and Kopp found that the reduced pressure coefficient,

$$C_p{}^* = \frac{\bar{C}_p - \bar{C}_{p,\min}}{1 - \bar{C}_{p,\min}} \tag{5}$$

(Roshko and Lau, 1965) at the mean reattachment point, $C_{p,Xr}{}^*$, varies with turbulence intensity and the aspect ratio of the windward wall, where $\bar{C}_{p,\min}$ is the minimum value of the mean pressure coefficient beneath the separated flow. Using $C_{p,Xr}{}^*$ from the data of Akon and Kopp along with $\bar{C}_{p,\min}$ from the current data, the value of $\bar{C}_p$ at the mean reattachment point can be estimated. From these, the mean reattachment length, X_r, at $z/H = 0.65$ can be assessed from the data in Fig. 12(c). Examining the mean pressure distributions in Fig. 12(c), full pressure recovery clearly occurs for $D/B > 4$, while, based on the estimates from the model of Akon and Kopp (2016), the mean reattachment point occurs at $d/B \approx 2$, i.e., the mean reattachment length, X_r, is about $2B$. This suggests that the mean flow is certainly reattached for D/B ratios greater than 2.5, consistent with the findings of Amin and Ahuja (2014). For $D/B < 2$, the pressure distributions are similar, but cut-off at the leeward edge of the body. Comparing the values of the pressure coefficients closest to the trailing edge (in Fig. 12c) with those on the leeward face (in Fig. 12b), it is clear the two are linked, unsurprisingly. Thus, the leeward wall pressure coefficients depend on the state of the separated flow from the windward wall edge and whether that flow is reattached and is fully recovered. Examining Fig. 11, the distributions over the entire side walls indicate that the mean reattachment length is longest over roughly the central heights of the building, $z/H = 0.2$ to 0.8, with decreased lengths near the roof and near the ground. For $D/B \leq 1$, the flow is fully separated and the mean pressure distributions are approximately uniform for each case, but dependent on the D/B ratio.

The fluctuating (C_p') distributions shown in Fig. 12(c) for $D/B \geq 1$ at $z/H = 0.65$ have a different shape from the $\bar{C}_p$ distributions. For example, while the mean pressure coefficients have their largest magnitudes at about $d/B = 0.6$, the C_p' distributions have their maxima at $d/B \approx 1.4$ for the reattached cases. Beyond the location of the maximum values of C_p', at roughly $d/X_r = 0.7$, the distributions for all configurations are the same, while for $D/B \geq 2.5$, where the mean flow is reattached, the distributions are the same, right from the leading edge. For $D/B \leq 1$, the flow is fully separated and the pressure fluctuations are fairly uniform on the side wall with largest values for $D/B = 0.67$ to 1. This is easiest to see in Fig. 11(b). For $D/B \geq 2.5$ the location of the peak fluctuations away from the edge is most visible (in Fig. 11b). The effects of the difference in the mean and fluctuating pressures on the peaks will be examined in Section 5.

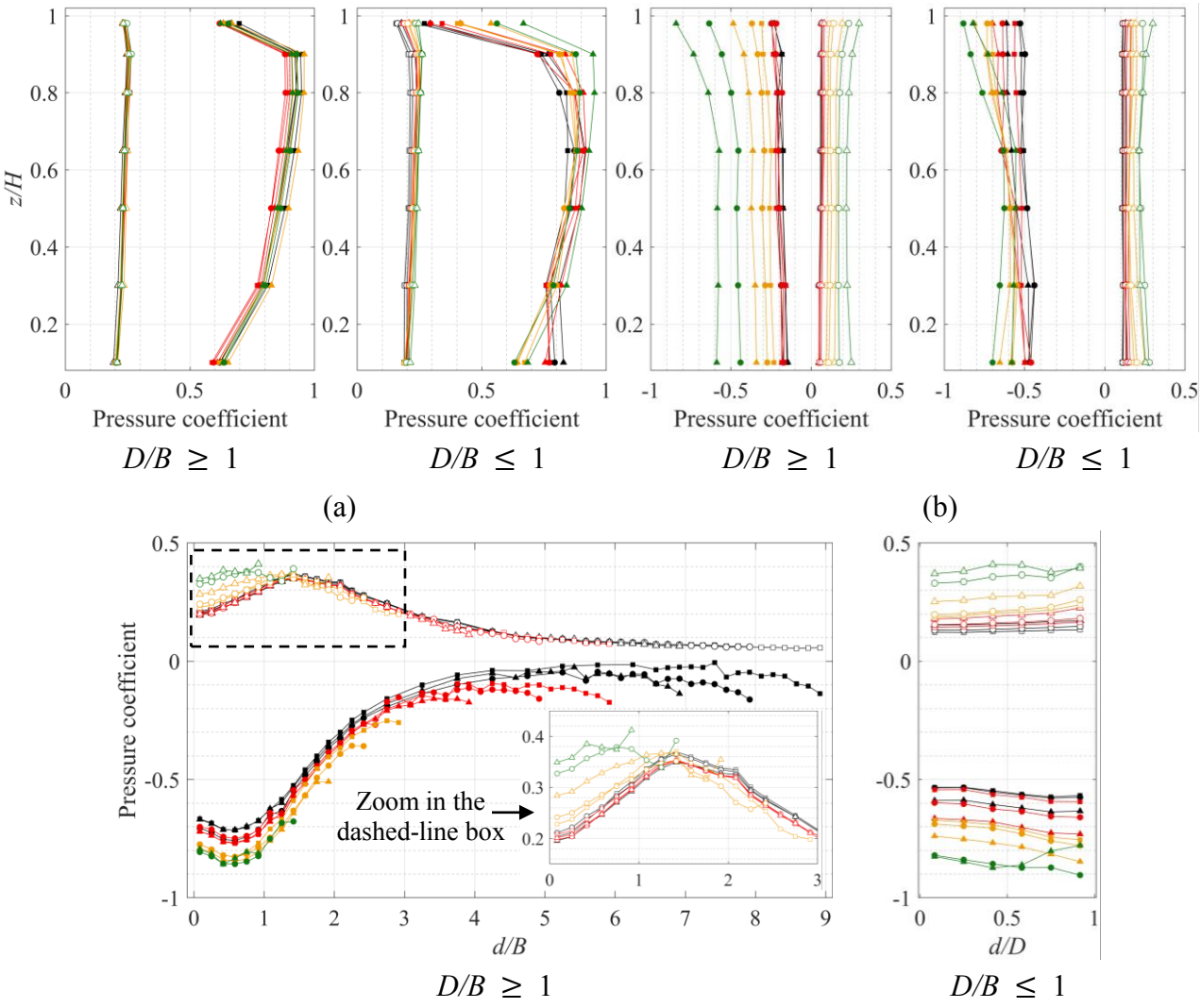

Fig. 12. $\bar{C}_p$ and C'_p on the (a) windward wall along the vertical centerline, (b) leeward wall along the vertical centerline, (c) side wall at $z/H = 0.65$, where d is the distance from leading edge. Data markers: $\bar{C}_p$ and C'_p use the same marker shape and color for each D/B configuration, but are represented by solid markers and open markers, respectively. For each D/B configuration: $D/B = 9$, $D/B = 8$, $D/B = 7$, $D/B = 6$, $D/B = 5$, $D/B = 4$, $D/B = 3$, $D/B = 2.5$, $D/B = 2$, $D/B = 1.5$, $D/B = 1$, configurations of $D/B \leq 1$ use the same markers as their reciprocals.

4 Area-averaged pressure coefficients

4.1 MWFRS loads in ASCE 7-16

In ASCE 7-16, the design wind pressures for the MWFRS of enclosed or partially enclosed rigid buildings of all heights are given by:

$$p_{ASCE} = q_z G C_{pe} = 0.5 \rho K_z K_{zt} K_d V^2 \cdot G C_{pe} \tag{6}$$

where p_{ASCE} is the equivalent static wind pressure, i.e., the pressure when statically applied to the

building will cause its maximum along-wind response (Solari and Kareem, 1998); q_z is the velocity pressure evaluated at height, z; ρ is the air density; K_z is velocity pressure exposure coefficient; K_{zt} and K_d are the topographic and wind directionality factors, respectively, both of which are assumed to be 1.0 in this study; V is the basic wind speed, corresponding to a 3-sec gust speed at 10 m above ground in open country terrain; G is the gust-effect factor, and C_{pe} is the external pressure coefficient. For windward walls, q_z is used, while for leeward walls, side walls, and roofs, q_H is used. It should be noted that internal pressures do not affect net horizontal loads and are not considered herein. The values for C_{pe}, provided in Table 3, are mean values since all gust effects are captured by G, as discussed further below. The MWFRS loads are for the design of the structural system, so they represent the loads acting on multiple external surfaces simultaneously. So, while these loads are provided for entire walls, these are used with load cases where the pressures are applied simultaneously to multiple surfaces. In contrast, the design loads for components attached to a single wall would fall under the provisions for components and cladding.

Table 3 External pressure coefficient stipulated in ASCE 7-16

Surface	*D/B*	C_{pe}	Use with
Windward Wall	All values	0.8	q_z
Leeward Wall	0 - 1	-0.5	q_H
	2	-0.3	
	≥4	-0.2	
Side Wall	All values	-0.7	q_H

In ASCE 7-16, the velocity pressure at height z, q_z, is calculated using the 3-sec gust wind speed at height z, instead of the mean wind speed. According to Solari and Kareem (1998), the gust-effect factor $G = G_Y/G_P$, where G_P is the gust pressure factor, which represents the conversion factor for dynamic pressure from the mean wind speed to the peak wind speed, i.e., the 3-sec gust wind speed (Solari, 1993a); and G_Y is the gust response factor, represents the effects of wind-induced response caused by gust-buffeting (Solari, 1993b) (for rigid buildings, only the background responses are considered). This implies that, the effects of using the 3-sec gust speed (instead of the mean speed) has been accounted for in the gust effect factor, G. Thus, C_{pe} should be the pressure coefficient referenced to dynamic pressure calculated from the mean wind speed. In the comparison between wind tunnel data and ASCE 7-16, the mean area-averaged pressure coefficients are used in the analysis.

The design pressures in ASCE 7-16 are applied to the building as particular load cases, which are provided in Figure 27.3-8 of the standard. Of particular interest are Cases 1 and 3, which are related to wall pressure coefficients, and are repeated here for convenience, as shown in Fig. 13,

where $C_{pe,W}$ and $C_{pe,L}$ are the external pressure coefficients on the windward wall and leeward wall, respectively. It should be noted that in ASCE 7-16, the wind directions for the design load cases are related to the principal axes of the structure, which are perpendicular to the walls for Load Case 1, corresponding to the wind directions of 0° and 90° in the current study. Load Case 3 pertains to oblique wind directions. Note that the torsional load cases are not examined herein.

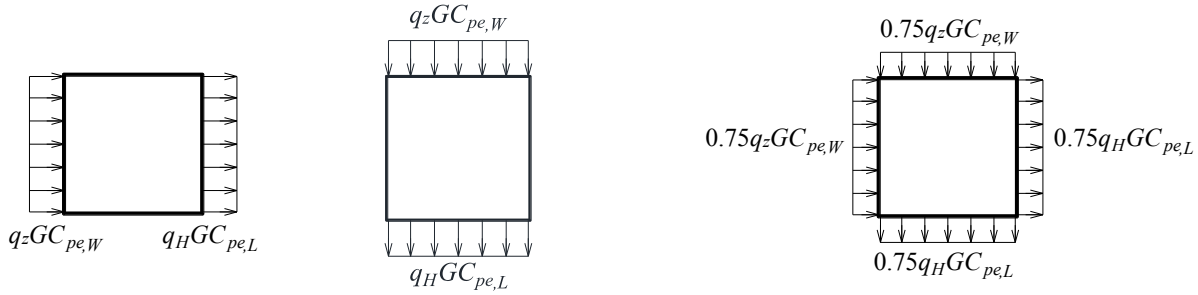

(a) (b)

Fig. 13 Design wind load cases in ASCE 7-16: (a) Load Case 1 and (b) Load Case 3.

4.2 Area-averaged MWFRS loads

Area-averaged pressure coefficients can be calculated by integrating the pressure coefficients over the building surfaces considering that pressure acts normal to the surface and is defined as positive when acting towards the surface. For pressure measured at discrete points, the area-averaged coefficient is defined as:

$$C_{pA}(t) = \sum_{i=1}^{N} C_{pi}(t)\frac{A_i}{A} \tag{7}$$

where A_i is the area of a pressure tap (as also represented by each color box in Fig. 9 to Fig. 11), A is the wall area. Note that, on the windward wall, as stipulated in ASCE 7-16, q_z is used in calculating p_{ASCE}, so C_{pe} is the mean pressure coefficient referenced to dynamic pressure at height, z. Thus, $\bar{C}_{pL}$ is used instead of $\bar{C}_p$, which is denoted by $\bar{C}_{pLA}$ for area-averages.

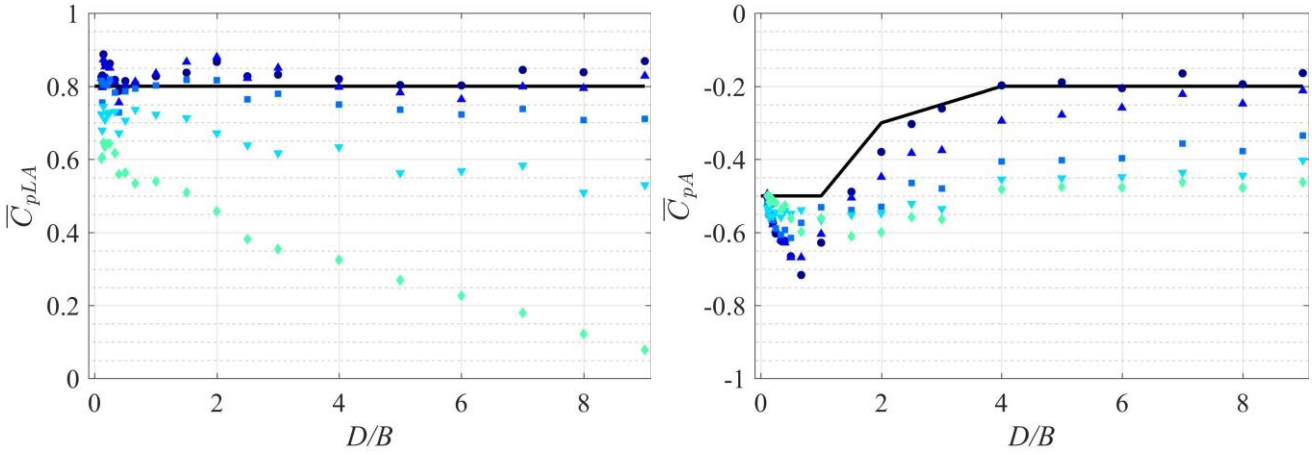

(a) (b)

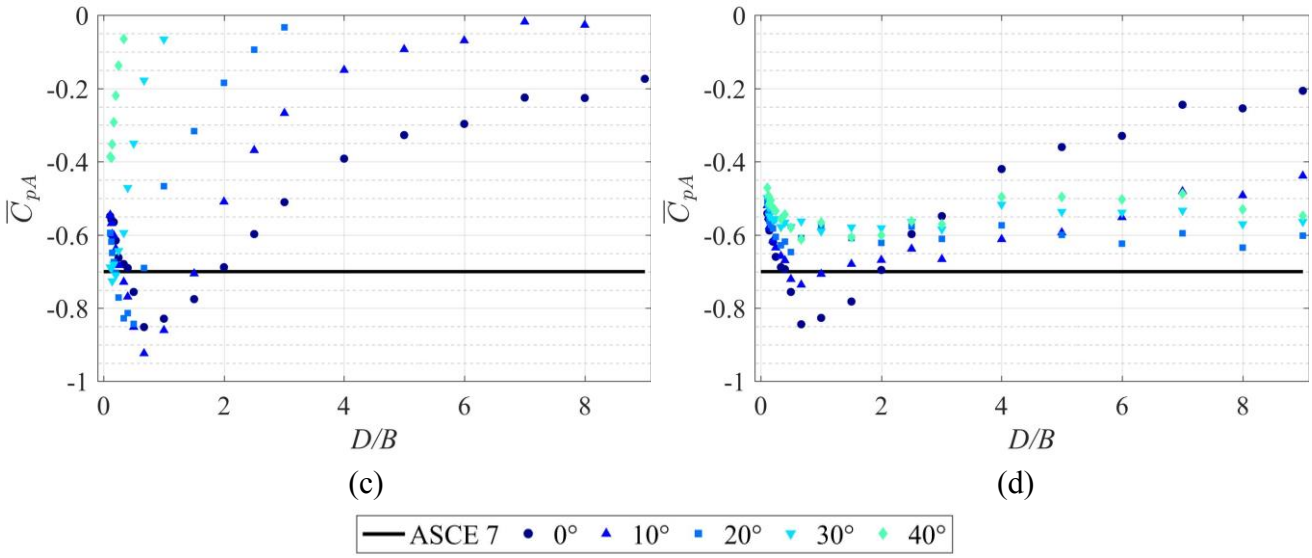

Fig. 14. Comparison between wind tunnel data $\bar{C}_{pA}$ (or $\bar{C}_{pLA}$) with C_{pe} in ASCE 7-16 on the (a) windward wall, (b) leeward wall, (c) more-windward side wall and (d) more-leeward side wall (as defined in Fig. 2).

Fig. 14 depicts the area-averaged pressure coefficients, $\bar{C}_{pA}$ (for side and leeward walls) and $\bar{C}_{pLA}$ (for the windward walls), as well as the C_{pe} values from ASCE 7-16 (provided in Table 3). The effects of wind direction are also shown in the figure. In addition to the orthogonal wind directions，wind directions extending 45° in either direction are provided (but, due to the symmetry of the building, only data in one direction are plotted).

From Fig. 14 it can be seen that, on the windward wall, the worst $\bar{C}_{pLA}$ are nearly constant for all *D/B* ratios, and the differences between the wind tunnel data and the ASCE 7-16 values are within 10%. The maximum values tend to occur for orthogonal wind directions, with smaller maxima for oblique wind directions. Note that for heights lower than 0.6*H* in the wind tunnel velocity profile, measured wind speeds are slightly higher than ESDU profiles. This implies that, based on the quasi-steady assumption, if the measured profiles matched perfectly with the target profiles, the true area-averages would be slightly smaller than the actual measured data. This would lead to the coefficients that are about 7% lower than those presented here. Thus, it is apparent that the maximum windward wall pressure coefficients provided in ASCE 7-16 are appropriate.

On the leeward wall, the minimum of the negative $\bar{C}_{pA}$ values is for *D/B* = 0.67 under the orthogonal wind direction with a value of about -0.7. For the orthogonal wind direction, $\bar{C}_{pA}$ is reduced in magnitude for both larger and smaller *D/B* ratios, as discussed in the previous section. For $D/B \geq 2.5$, wind tunnel data on the leeward wall fit well with ASCE 7-16, but for $D/B < 2.5$, the provisions are smaller in magnitude. However, the critical wind directions shift away from the orthogonal direction for $D/B > 1$, leading to much larger magnitude coefficients in the measured data than in the ASCE provisions. For MWFRS loads, which consider the actions on the complete

structure, it is not clear what the implications of these underestimates would be. To examine this point, the mean base shear coefficients in the x direction, $\bar{C}_{BFx}$, are compared, where C_{BFx} is calculated as:

$$C_{BFx}(t) = C_{pA,W}(t) - C_{pA,L}(t) \tag{8}$$

where $C_{pA,W}$ and $C_{pA,L}$ are the area-averaged pressure coefficients on the windward and leeward walls, respectively.

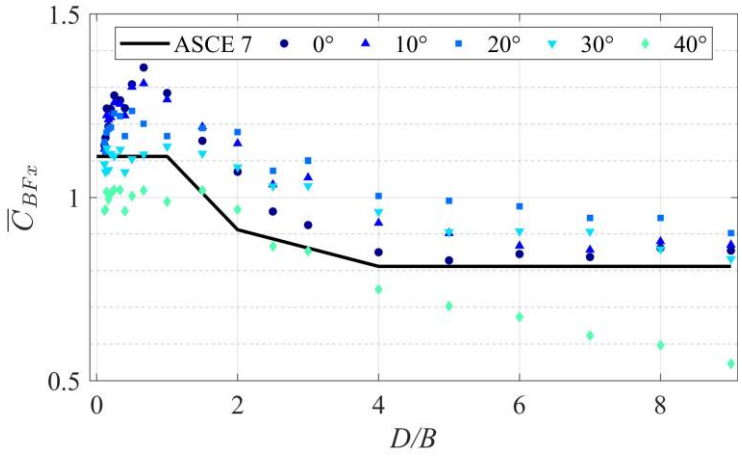

Fig. 15. Mean base shear coefficients, $\bar{C}_{BFx}$, as a function of *D/B* ratio and wind direction.

The measured values of $\bar{C}_{BFx}$ for the different wind directions are given in Fig. 15, together with the ASCE 7-16 values. Note that the ASCE 7-16 value in the figure is not simply the sum of $C_{pe,W}$ and $C_{pe,L}$, as different velocity pressures (i.e., q_z for windward wall and q_H for leeward wall) should be used when calculating the design wind pressures. In light of this, $C_{pe,W}$ has been multiplied by a conversion factor and converted to an equivalent value $C_{pe,WE}$, which corresponds to q_H, based on the following equation:

$$C_{pe,WE}(t) = F_c * C_{pe,W} = \frac{\int_0^H \left(\frac{z}{10}\right)^{2\bar{\alpha}} \mathrm{d}z}{H * \left(\frac{H}{10}\right)^{2\bar{\alpha}}} * C_{pe,W} \tag{9}$$

where $\bar{\alpha}$ is the power law exponent of the mean wind speed profile for Exposure C in ASCE 7-16, and the conversion factor, F_c, is found to be 0.76. The ASCE 7-16 value in Fig. 15 is the sum of $\bar{C}_{pe,WE}$ and $\bar{C}_{pe,L}$, which corresponds to the definition of $\bar{C}_{BFx}$. It is observed that the largest $\bar{C}_{BFx}$ occurs for *D/B* = 0.67, with large values in the range of 0.5 to 1, but decreasing for larger or smaller *D/B* ratios. Besides, the most unfavorable wind direction is the orthogonal wind direction for $D/B \leq 1$, 10° from the orthogonal for *D/B* = 1.5, and is 20° for $D/B \geq 2$. Thus, if all wind directions are considered, it would be more appropriate if C_{pe} for the leeward wall was -0.5 for very small *D/B* ratios, -0.7 for *D/B* = 0.67, -0.6 for *D/B* = 1 and -0.3 for $D/B \geq 4$ (with linear interpolation between these *D/B* ratios), as also listed in Table 4.

For the side walls, the largest magnitude $\bar{C}_{pA}$ value also occurs for *D/B* = 0.67 for a wind direction of 10°, reaching a value of about -0.9 in Fig. 14. Values of $\bar{C}_{pA}$ greater in magnitude than ASCE 7-16 suction coefficient of 0.7 appear for *D/B* = 0.33 to 1.5. It is also observed that for *D/B* ≥ 4, $\bar{C}_{pA}$, the worst side wall minima are about -0.60. More appropriate design values are listed in Table 4, note that for *D/B* ratios other than shown in the table, values of C_{pe} can be obtained by linear interpolation.

Table 4 Recommended design values of C_{pe}

D/B	Windward Wall	Leeward Wall	Side Wall
0.1	0.8	-0.5	-0.6
0.67		-0.7	-0.8
1		-0.6	
2		-0.5	-0.7
≥4		-0.3	-0.6
Use With	q_z	q_H	q_H

5 Peak point pressure distributions

As discussed in the previous section, the design wind pressure, p_{ASCE}, takes into account the effects of wind gustiness and structural dynamics. For rigid buildings, the latter is ignored such that the design pressure is a peak pressure. The design wind speed in ASCE 7-16 corresponds to a peak gust speed such that the effects of wind gustiness are implicitly included. Peak pressure coefficients are defined as:

$$\hat{C}_p = \frac{\hat{P} - P_\infty}{0.5\rho\hat{U}_H{}^2} \tag{10}$$

where $\hat{P}$ is the peak wind pressure and $\hat{U}_H$ is the peak wind speed at the roof height, *H*. The minimum pressure coefficient, $\check{C}_p$, is defined similarly using the peak gust speed. $\hat{U}_H$ is obtained by:

$$\hat{U}_H = (1 + gI_{uH})\,\overline{U}_H \tag{11}$$

where g is the peak factor, I_{uH} is the turbulence intensity at roof height, *H*. A value of g = 3 is used, corresponds to the value from mean-hourly wind speed to 3 sec gust speed (ESDU, 1985).

In ASCE 7-16, $\hat{C}_p$, corresponds to the product of *G* and C_{pe}, where *G* is the gust effect factor. As discussed in Solari and Kareem (1998), for rigid buildings, *G* incorporates the effects of spatial averaging and the lack of contemporaneous gust action, divided by the effect of wind gustiness, which can result in *G* < 1 (Solari and Kareem, 1998). For point-like structures (or for a single pressure measurement point), there is no effect of spatial averaging such that *G* = 1. However, as can

be seen in Solari and Kareem (1998) and Solari (1993a), in the formulation of G, only the wind gustiness is considered while the smaller-scale body-generated turbulence is neglected. If the quasi-steady theory holds, the peak pressure coefficient $\hat{C}_p$ will have the same value as the quasi-steady pressure coefficient, i.e., the mean pressure coefficient, $\bar{C}_p$. However, due to existence of body-generated turbulence, there will be differences between $\hat{C}_p$ and $\bar{C}_p$. Thus, both spatial-averaging and the effects of body-generated turbulence will affect the true value of the peak pressure coefficient. The measured peak pressure coefficients ($\hat{C}_p$ for positive $\bar{C}_p$, and $\check{C}_p$, for negative $\bar{C}_p$) are examined in this section.

There are several methods to estimate peak values, as recently summarized by Gavanski et al. (2016). In this study, the Lieblein BLUE method (Lieblein, 1974) is used to determine the extreme values of the peak pressure coefficients. In this method, the time series data are divided into 10 equal segments and the maxima (or minima) are obtained for each. The resulting mean values of the Gumbel distribution are presented. Fig. 16, Fig. 17 and Fig. 18 depict the distributions of $\hat{C}_p$ on the windward wall, and $\check{C}_p$ on the leeward and side walls under the orthogonal wind direction, respectively. Fig. 19 provides a comparison of $\bar{C}_p$ and $\hat{C}_p$ (or $\check{C}_p$).

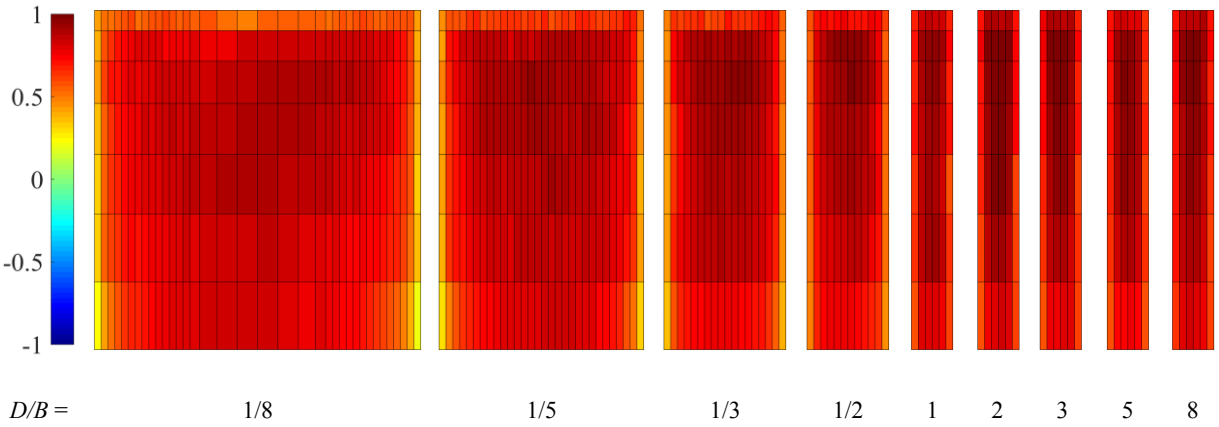

Fig. 16 Distributions of $\hat{C}_p$ on the windward wall under the orthogonal wind direction.

From Fig. 16 it can be seen that, on the windward wall, $\hat{C}_p$ distributions have similar patterns when compared to the $\bar{C}_p$ distributions shown in Fig. 9. However, the magnitudes are different, as can be seen in Fig. 19(a). It is apparent that, for these point pressure measurements, the peak pressure coefficients are larger than the mean coefficients. Furthermore, the differences are relatively larger near the edges, top and bottom of the buildings. These differences can be mainly attributed to the body-generated turbulence effects. In addition, the wind tunnel measured pressures are instantaneous values that are normalized by 3-sec gust speeds to obtain the peak pressure coefficients (see Equation 10). Thus, the larger peak pressure coefficients may also result from the effects of wind gusts of shorter duration than 3 seconds.

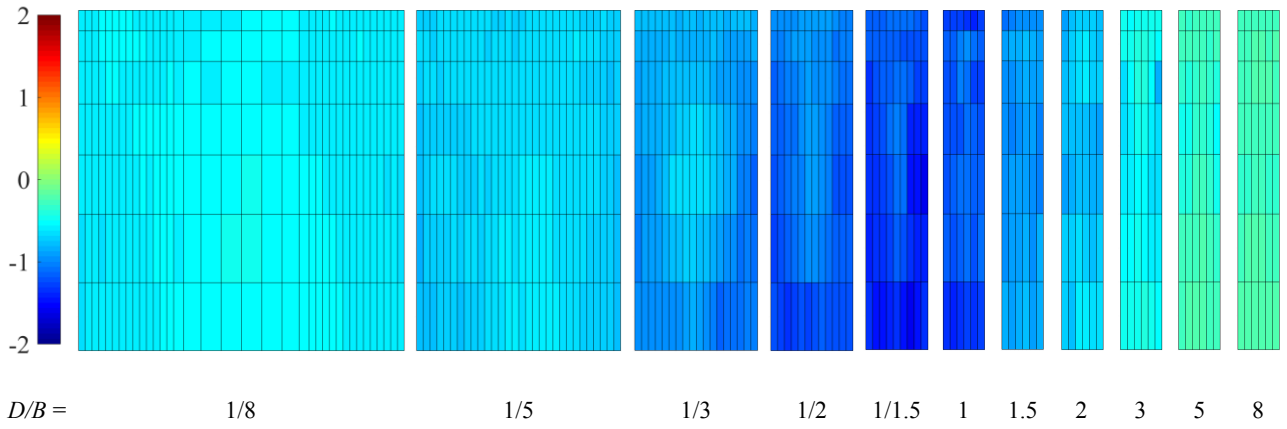

Fig. 17. Distributions of $\check{C}_p$ on the leeward wall under the orthogonal wind direction.

On the leeward wall, the peak $\check{C}_p$ distributions also have similar spatial patterns to the mean $\bar{C}_p$ distributions since $\check{C}_p$ does not vary much over each wall, for all *D/B* ratios. From Fig. 19(b), it can be seen that the magnitudes are substantially different with the peak coefficients being larger. The differences are largest for *D/B* ratios near 1. For the large or small *D/B* ratios, the relative differences become smaller.

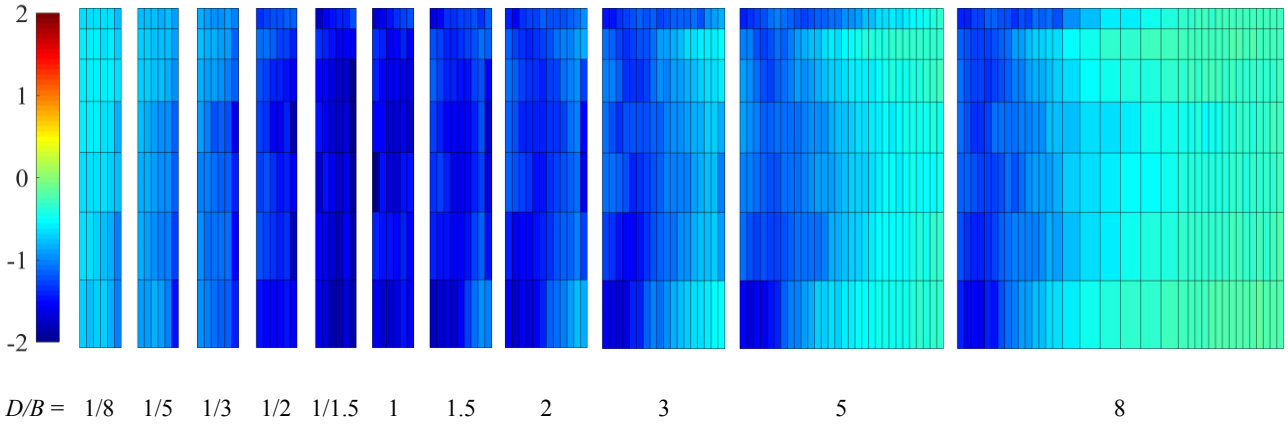

Fig. 18. Distributions of $\check{C}_p$ on the side walls under the orthogonal wind direction. Wind direction: from left to right.

For the side walls, the $\check{C}_p$ distributions have some similarities to the patterns for the $\bar{C}_p$ distributions. For *D/B* > 1, $\check{C}_p$ distributions near the leading edge are similar. However, $\check{C}_p$ near the trailing edge becomes more negative abruptly and dramatically for building mid-heights with $D/B \leq 4$, which can be most clearly seen in Fig. 19(c). For the magnitudes, there are large differences between $\check{C}_p$ and the mean coefficient, $\bar{C}_p$, with much larger magnitudes for the peak coefficients.

Again, these differences are most significant for D/B = 0.67 to 1.5. For larger and smaller D/B ratios, the differences are reduced but still significant even for D/B = 9 and 1/9.

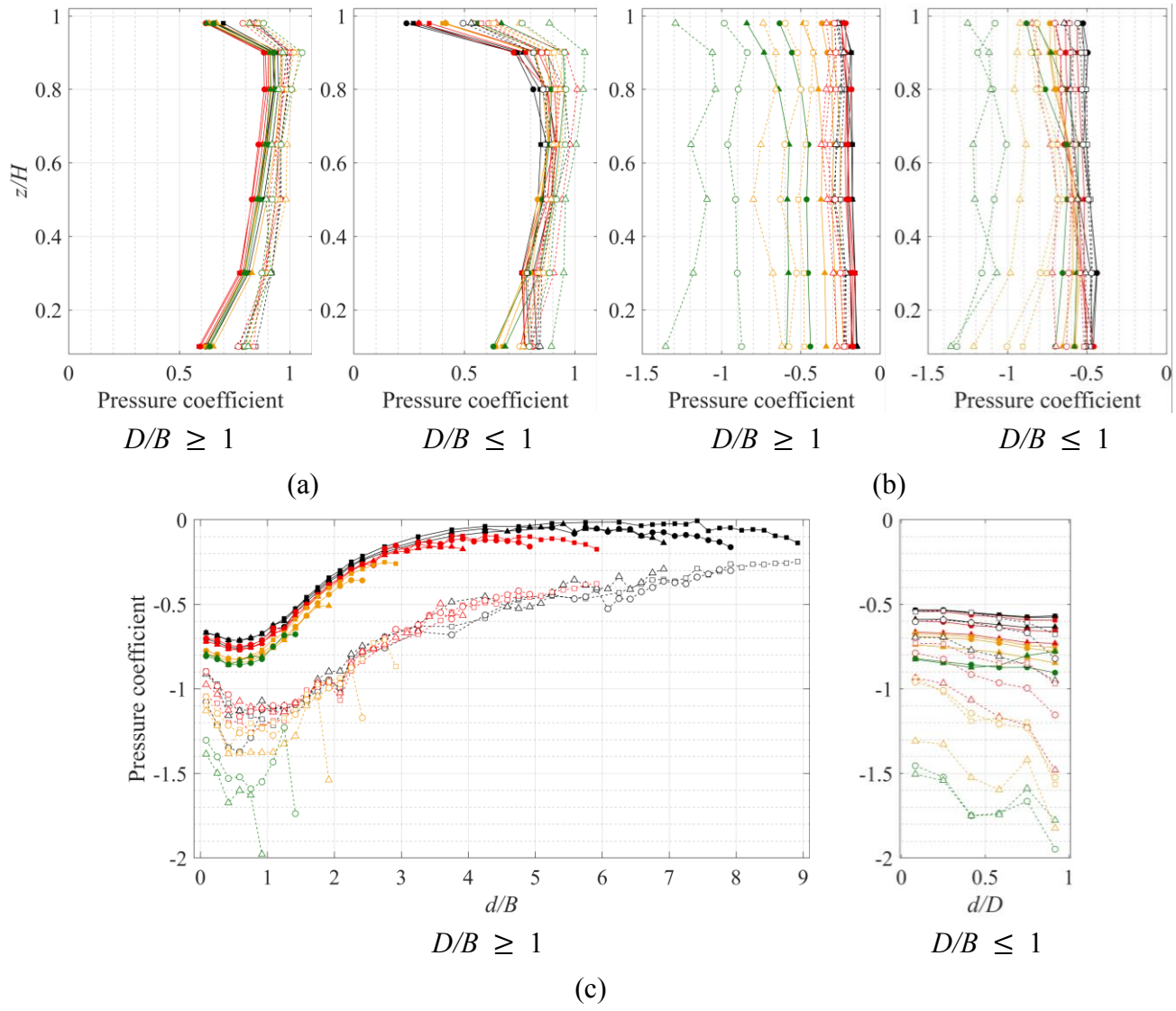

Fig. 19. $\bar{C}_p$ and $\hat{C}_p$ (for positive $\bar{C}_p$) or $\check{C}_p$ (for negative $\bar{C}_p$) on the (a) windward wall along the vertical centerline, (b) leeward wall along the vertical centerline, (c) side wall at z/H = 0.65, where d is the distance from leading edge. Data markers: $\bar{C}_p$ and $\hat{C}_p$ use the same marker shape and color for each D/B configuration, but are represented by solid line with solid markers and dashed line with open markers, respectively. For each D/B configuration: D/B = 9, D/B = 8, D/B = 7, D/B = 6, D/B = 5, D/B = 4, D/B = 3, D/B = 2.5, D/B = 2, D/B = 1.5, D/B = 1, configurations of $D/B \leq 1$ use the same markers as their reciprocals.

6 Comparison between area-averaged mean and peak pressure coefficients

As discussed in the previous section, the quasi-steady pressure coefficient will usually underestimate the point pressure due to the existence of small-scale body-generated turbulence and/or gusts of shorter duration than 3 seconds. The effects of small-scale body-generated turbulence are eliminated by the area-averaging process, while filtering of the upstream turbulence also improves the quasi-steady modeling because of a lack of correlation between the surface pressures and the smaller-scale gusts (Wu, 2017). This means that the quasi-steady theory will work better for area-averages than for a single pressure tap, as shown recently by the work of Wu and Kopp (2016), which makes it useful as the basis for MWFRS wind loads in building codes (Solari, 1993a; Solari and Kareem, 1998). In this section, the area-averaging process is conducted using Equation (7), while the peak values of $C_{pA}(t)$ (or $C_{pLA}(t)$ for the windward wall) are estimated based on the method described in section 5.

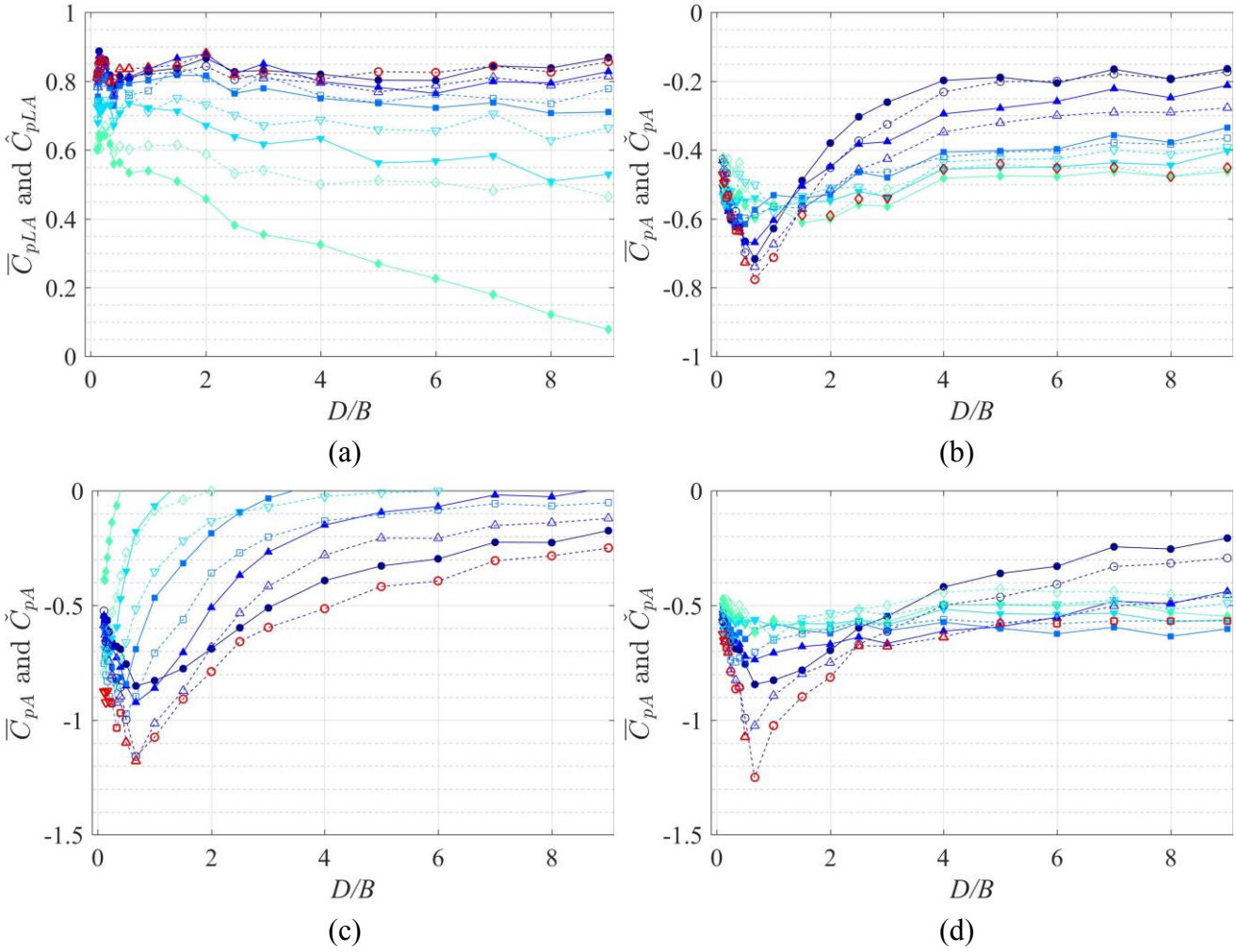

Fig. 20 (a) $\bar{C}_{pLA}$ and $\hat{C}_{pLA}$ on the windward wall and $\bar{C}_{pA}$ and $\check{C}_{pA}$ on the (b) leeward wall, (c) more-windward side wall, and (d) more-leeward side wall (as defined in Fig. 2). Data markers: 0°, 10°, 20°, 30°, 40°; solid markers represent $\bar{C}_{pLA}$ or $\bar{C}_{pA}$, while open markers

represent $\hat{C}_{pLA}$ or $\check{C}_{pA}$; red markers represent the worst $\hat{C}_{pLA}$ or $\check{C}_{pA}$.

Fig. 20 shows the comparison between $\bar{C}_{pA}$ and $\check{C}_{pA}$ (or $\bar{C}_{pLA}$ and $\hat{C}_{pLA}$ for the windward wall). Overall, the differences between area-averages, i.e., $\bar{C}_{pA}$ and $\check{C}_{pA}$, are much smaller when compared to the point pressure coefficients, i.e., $\bar{C}_p$ and $\check{C}_p$.

On the windward wall, the worst $\hat{C}_{pLA}$ are approximately constant for all *D/B* ratios, and the critical wind directions usually occur at 0° or 10°. Under the critical wind directions, values of $\bar{C}_{pLA}$ and $\hat{C}_{pLA}$ are similar. For *D/B* > 0.5 under oblique wind directions larger than 30°, $\hat{C}_{pLA}$ tends to deviate from $\bar{C}_{pLA}$, and the differences tend to be more obvious for larger wind angles or larger *D/B* ratios.

On the leeward wall, the worst $\check{C}_{pA}$ occurs at *D/B* = 0.67 under the orthogonal wind direction, as it does for $\bar{C}_{pA}$. The critical wind directions change gradually from 0° to 30° as *D/B* is reduced from 1 to 0.11, and change to 40° for $D/B \geq 1.5$. Under the critical wind directions, $\bar{C}_{pA}$ is usually smaller than $\check{C}_{pA}$ in magnitude for $0.25 < D/B \leq 1$, but is usually slightly larger (in magnitude) for $D/B \geq 1.5$. This may due to the fact that both the unsteadiness of the wake and the effects of the upstream turbulence on the leeward wall are reduced as the *D/B* ratio increases.

On the side wall, the worst $\check{C}_{pA}$ is about -1.25 and also occurs for $D/B = 0.67$ on the more-leeward side, under the orthogonal wind direction. On the more-windward side, critical wind directions occur at 20° and 30° for *D/B* < 0.25, 10° for $0.5 \leq D/B < 1$, and usually occur at 0° for $D/B \geq 1$. It also can be seen that, under these critical wind directions, $\bar{C}_{pA}$ is usually smaller in magnitude than $\check{C}_{pA}$ by about 30%, which is much more significant than on the windward and leeward walls. On the more-leeward side, critical wind directions usually occur at 0° for *D/B* < 2.5, and gradually shift to 20° for larger *D/B* ratios. Under these critical wind directions, $\bar{C}_{pA}$ is usually smaller in magnitude than $\check{C}_{pA}$ for *D/B* < 2.5, especially for $0.5 \leq D/B < 1.5$, while it matches well or is slightly larger for $D/B \geq 2.5$ (corresponding to the reattachment cases discussed in section 3).

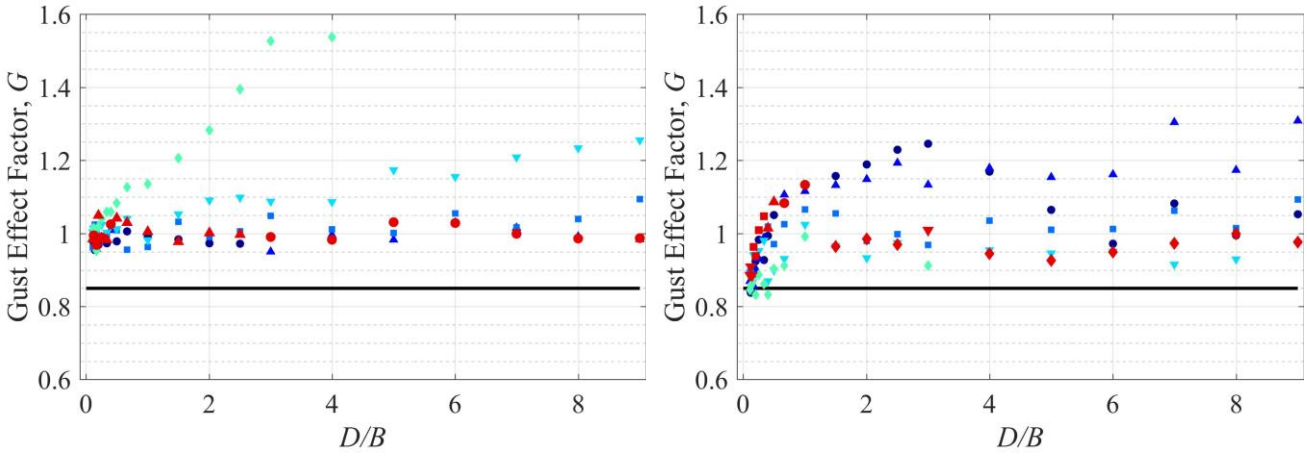

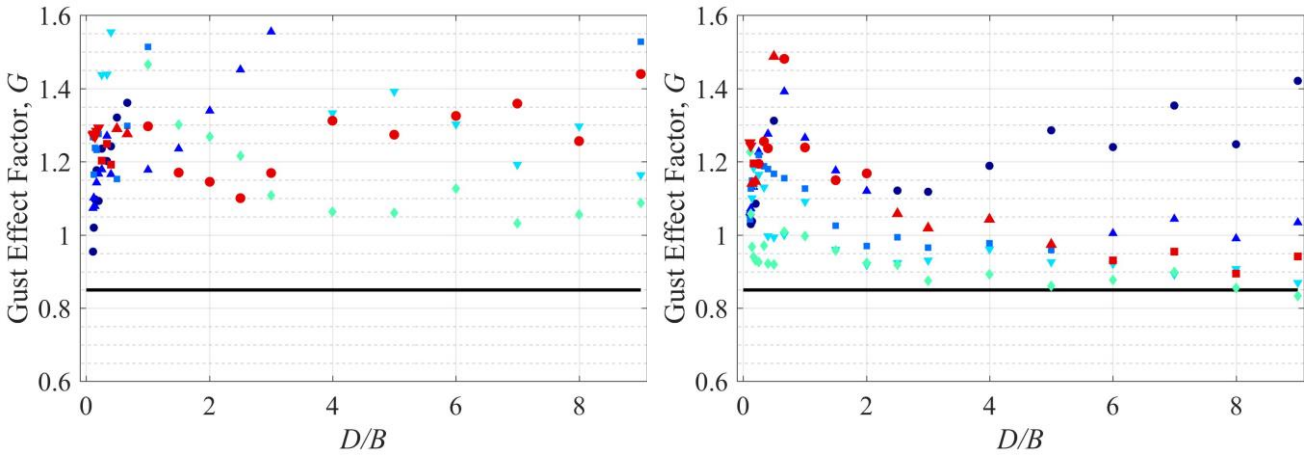

Fig. 21 Comparison between gust effect factor, G, from wind tunnel area-averaged pressure coefficients and ASCE 7-16 on the (a) windward wall, (b) leeward wall, (c) more-windward side wall and (d) more-leeward side wall (as defined in Fig. 2). Data markers: — ASCE 7, • 0°, ▲ 10°, ■ 20°, ▼ 30°, ♦ 40°; red markers represent G for the worst $\hat{C}_{pLA}$ or $\check{C}_{pA}$.

Comparisons between the gust effect factor, G, from wind tunnel area-averaged pressure coefficients and ASCE 7-16 are shown in Fig. 21. For rigid buildings, the value of G for ASCE 7-16 can be taken as 0.85, and G for wind tunnel data can be calculated by:

$$G = \frac{\check{C}_{pA}}{\bar{C}_{pA}} \tag{12}$$

where, for the windward wall, $\bar{C}_{pLA}$ and $\hat{C}_{pLA}$ should be used instead, as discussed above. Note that the effects of wind gustiness have already been included in $\check{C}_{pA}$, as defined by Equation (10).

As can be seen in Fig. 21, overall, the measured values of G are usually higher than the ASCE 7-16 value of 0.85. Similar to the discussion above, under critical wind directions (i.e., where the worst $\hat{C}_{pLA}$ or $\check{C}_{pA}$ occurs), G is close to unity on the windward wall, while on the leeward wall, G is usually larger than 1 for $0.5 \leq D/B < 1.5$ and smaller than 1 for $D/B \geq 1.5$. On the more-windward side wall, G is always higher than 1, and reaches a value of 1.3 under critical wind directions, while on the more-leeward side, G is larger than unity for $D/B < 2.5$ while near or slightly smaller than unity for $D/B \geq 2.5$.

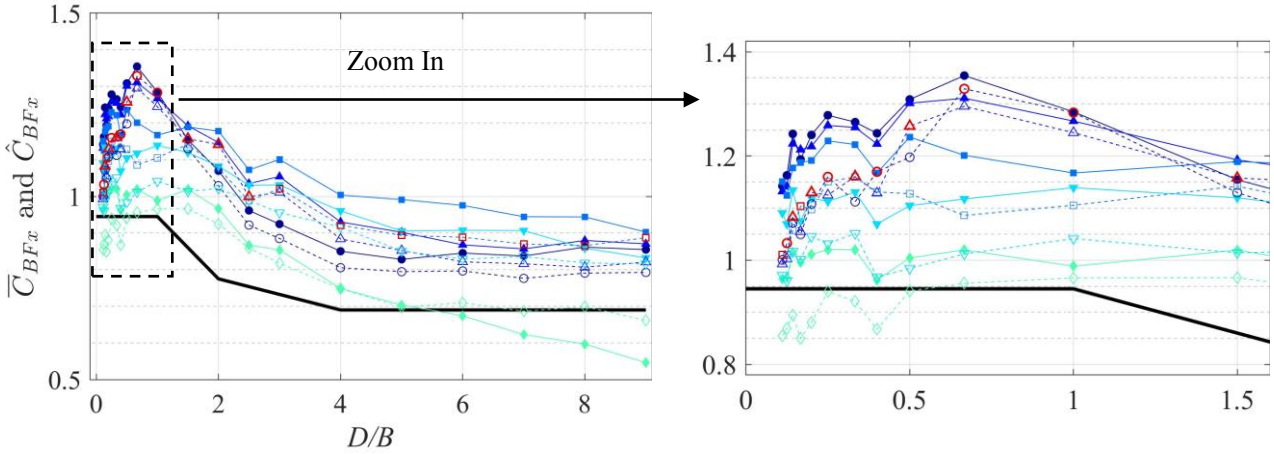

Fig. 22 $\bar{C}_{BFx}$ and $\hat{C}_{BFx}$, as a function of *D/B* ratio and wind direction, and comparison with peak base shear coefficient in ASCE 7-16. Data markers: ASCE 7, 0°, 10°, 20°, 30°, 40°; solid markers represent $\bar{C}_{BFx}$, while open markers represent $\hat{C}_{BFx}$; red markers represent the worst $\hat{C}_{BFx}$.

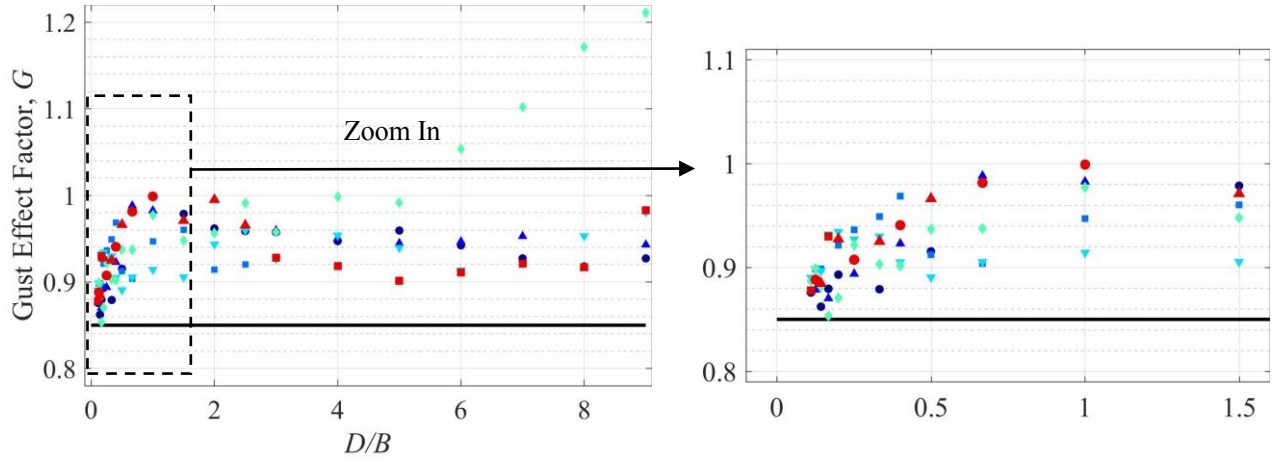

Fig. 23 Comparison between gust effect factor, *G*, from wind tunnel base shear coefficients and ASCE 7-16. Data markers: ASCE 7, 0°, 10°, 20°, 30°, 40°; red markers represent *G* for the worst $\hat{C}_{BFx}$.

Fig. 22 shows the comparison between mean base shear coefficient, $\bar{C}_{BFx}$, and peak base shear coefficient, $\hat{C}_{BFx}$, and Fig. 23 shows the comparisons between *G* from the wind tunnel base shear coefficients and ASCE 7-16, where *G* is calculated in the same way as Equation (12). It can be seen that, the critical wind directions usually occur at 0° or 10° for $D/B < 2.5$, and shift to 20° for $D/B \geq 2.5$. Under the critical wind directions, the overall $\hat{C}_{BFx}$ is about 40% larger than the ASCE 7-16 provisions for $D/B \geq 0.5$, and the value of $\hat{C}_{BFx}$ is usually smaller than $\bar{C}_{BFx}$. The value of *G*, under the critical wind directions, reaches values near 1 for $0.67 \leq D/B \leq 2$, with slight reductions to about 0.9 for larger *D/B* ratios. However, these values are always higher than the ASCE 7-16 value of 0.85. Thus, the larger magnitude of $\hat{C}_{BFx}$ is due to a combination of both the larger $\bar{C}_{pA}$ on the

leeward wall for all *D/B* ratios and the larger *G*, whose more appropriate design values would be 0.85 for very small *D/B* ratios, 1 for $0.67 \leq D/B \leq 2$, and 0.9 for $D/B \geq 4$, as listed in Table 5.

Table 5 Recommended design values of *G*

D/B	*G*
0.1	0.85
0.67 - 2	1
≥4	0.9

7 Conclusions

The objective of this research is to systematically investigate the effects of plan dimensions on wind loads acting on rigid rectangular high-rise buildings. Comparisons with ASCE 7-16 provisions are also made using scale-model wind tunnel tests. The following conclusions can be drawn:

(1) Mean pressure distributions on the windward are similar for all plan ratios. On the leeward wall, mean pressure distributions are relatively uniform, and the most unfavorable plan ratios are 0.5 to 1, the overall mean pressure coefficient becomes less negative as plan ratio decreases or increases. On the side walls, the most unfavorable plan ratios are 0.67 to 1.5, and the mean pressure distributions near the leading edge are close to being self-similar on the long side. Mean flow will reattach on the long side when plan ratio is larger than 2.5.

(2) A comparison for area-averaged mean pressure coefficients is made with ASCE 7-16. Mean pressure coefficients fit well with ASCE 7-16 on the windward wall, but are much larger in magnitude than the ASCE 7-16 provisions on the leeward wall if all wind directions are considered. On the side walls, mean pressure coefficients are larger in magnitude for plan ratios between 0.33 to 1.5.

(3) Peak pressure coefficients for single taps are close to mean pressure coefficients on the windward wall, but on the leeward and side walls, the differences between peak and mean pressure coefficients are large, reaching maxima for plan ratios of 0.67 to 1.5.

(4) The differences between the area-averaged mean and peak pressure coefficients are relatively small compared with point pressure coefficients. Mean values usually estimate peak values well under critical wind directions on the windward and leeward wall. On the more-windward side, mean values usually underestimate peak values by 30% under critical wind directions. On the more-leeward side, mean values usually underestimate peak values for plan ratios smaller than 2.5, while they match well or slightly overestimate the values for plan ratios larger than 2.5.

(5) The overall measured peak base shear coefficients under critical wind directions are about 40% larger than the ASCE 7-16 provisions for plan ratios larger than about 0.5. This is due to a

combination of both the mean pressure coefficients on the leeward wall for all plan ratios and the gust effect factors, which approach values of 1 for plan ratios between 0.67 to 2 for the rigid buildings considered in this study.

Acknowledgements

Y. Liu gratefully acknowledges financial support from the China Scholarship Council. G. A. Kopp acknowledges financial support for the wind tunnel experiments from the NSERC Discovery Grants program.

References

Akins, R. E., & Cermak, J. E. (1976). *Wind pressures on buildings*.

Akins, R. E., Peterka, J. A., & Cermak, J. E. (1977). Mean Force and Moment Coefficients for Buildings in. *Journal of Wind Engineering and Industrial Aerodynamics*, *2*(3), 195–209.

Akins, R. E., Peterka, J. A., & Cermak, J. E. (1980). Averaged Pressure coefficient for Rectangular Buildings. *Wind Engineering*, 369–380.

Akon, A. F. (2017). Effects of turbulence on the separating-reattaching flow above surface-mounted, three-dimensional bluff bodies (Western University). Retrieved from http://ir.lib.uwo.ca/cgi/viewcontent.cgi?article=6173&context=etd

Akon, A. F., & Kopp, G. A. (2016). Mean pressure distributions and reattachment lengths for roof-separation bubbles on low-rise buildings. *Journal of Wind Engineering and Industrial Aerodynamics*, *155*, 115–125. https://doi.org/10.1016/j.jweia.2016.05.008

Ali, M. M., & Moon, K. S. (2007). Structural Developments in Tall Buildings: Current Trends and Future Prospects. *Architectural Science Review*, *50*(3), 205–223. Retrieved from http://dx.doi.org/10.3763/asre.2007.5027

American Society of Civil Engineers (ASCE). (1993). ASCE Standard, Minimum Design Loads for Buildings and Other Structures. ASCE 7-93.

American Society of Civil Engineers (ASCE). (2012). ASCE Standard, Wind tunnel testing for buildings and other structures. ASCE 49-12.

American Society of Civil Engineers (ASCE). (2016). ASCE Standard, Minimum Design Loads for Buildings and Other Structures. ASCE 7-16.

Amin, J. A., & Ahuja, A. K. (2014). Characteristics of wind forces and responses of rectangular tall buildings. *International Journal of Advanced Structural Engineering*, *6*(3), 1–14. https://doi.org/10.1007/s40091-014-0066-1

Bearman, P. W., & Morel, T. (1983). Effect of free stream turbulence on the flow around bluff bodies. *Progress in Aerospace Sciences*, *20*(2–3), 97–123. https://doi.org/10.1016/0376-0421(83)90002-7

Cheung, J. C. K. (1984). Effect of tall building edge configurations on local surface wind pressures. *Proceedings of the 3rd International Conference on Tall Buildings*.

Dalgliesh, W. A. (1975). Comparison of model/full-scale wind pressures on a high-rise building. *Journal of Wind Engineering and Industrial Aerodynamics*, *1*, 55–66. https://doi.org/10.1016/0167-6105(75)90006-9

Diaz, P. S. Q. (2006). *Uncertainty analysis of surface pressure measurements on low-rise buildings*. The University of Western Ontario.

Engineering Science Data Unit (ESDU). (1974). Characteristics of atmosphere turbulence near the ground, Part 2: Single point data for strong winds (neutral atmosphere). Data Item 74031.

Engineering Science Data Unit (ESDU), (1982). Strong winds in the atmosphere boundary layer, Part 1: Mean-hourly wind speeds. Data Item 82026.

Engineering Science Data Unit (ESDU). (1985). Characteristics of atmosphere turbulence near the ground, Part 2: Single point data for strong winds (neutral atmosphere). Data Item 85020.

Gavanski, E., Gurley, K. R., & Kopp, G. A. (2016). Uncertainties in the Estimation of Local Peak Pressures on Low-Rise Buildings by Using the Gumbel Distribution Fitting Approach. *Journal of Structural Engineering*, *142*(11), 04016106. https://doi.org/10.1061/(asce)st.1943-541x.0001556

Ho, T. C. E., Surry, D., Morrish, D., & Kopp, G. A. (2005). The UWO contribution to the NIST aerodynamic database for wind loads on low buildings: Part 1. Archiving format and basic aerodynamic data. *Journal of Wind Engineering and Industrial Aerodynamics*, *93*(1), 1–30. https://doi.org/10.1016/j.jweia.2004.07.006

Hong, E. S. (2017). *Wall Pressure Coefficients for Low- to High-Rise Buildings*. Western University.

Kareem, A., & Cermak, J. E. (1984). Pressure fluctuations on a square building model in boundary-layer flows. *Journal of Wind Engineering and Industrial Aerodynamics*, *16*(1), 17–41. https://doi.org/10.1016/0167-6105(84)90047-3

Kim, Y., & Kanda, J. (2010). Characteristics of aerodynamic forces and pressures on square plan buildings with height variations. *Journal of Wind Engineering and Industrial Aerodynamics*, *98*(8–9), 449–465. https://doi.org/10.1016/j.jweia.2010.02.004

Kopp, G. A., & Morrison, M. J. (2018). Component and Cladding Wind Loads for Low-Slope Roofs on Low-Rise Buildings. *Journal of Structural Engineering*, *144*(4), 04018019. https://doi.org/10.1061/(asce)st.1943-541x.0001989

Lander, D. C., Letchford, C. W., Amitay, M., & Kopp, G. A. (2016). Influence of the bluff body shear layers on the wake of a square prism in a turbulent flow. *Physical Review Fluids*, *1*(4), 1–28. https://doi.org/10.1103/physrevfluids.1.044406

Lieblein, J. (1974). *Efficient methods of extreme-value methodology*.

Lin, N., Letchford, C., Tamura, Y., Liang, B., & Nakamura, O. (2005). Characteristics of wind forces acting on tall buildings. *Journal of Wind Engineering and Industrial Aerodynamics*, *93*(3), 217–242. https://doi.org/10.1016/j.jweia.2004.12.001

McClean, J. F., & Sumner, D. (2014). An Experimental Investigation of Aspect Ratio and Incidence Angle Effects for the Flow Around Surface-Mounted Finite-Height Square Prisms. *Journal of Fluids Engineering*, *136*(8), 081206. https://doi.org/10.1115/1.4027138

Melbourne, W. H. (1980). Comparison of measurements on the CAARC standard tall building model in simulated model wind flows. *Journal of Wind Engineering and Industrial Aerodynamics*, *6*(1–2), 73–88.

Miyoshi, S., Ida, M., & Miura, T. (1971). Wind Pressure Coefficients on Exterior Wall Elements of a

Tall Building. *Proceedings of the Third International Conference on Wind Effects on Buildings and Structures*, 273–284.

Nakamura, Y., & Hirata, K. (1989). Critical geometry of oscillating bluff bodies. *Journal of Fluid Mechanics*, *208*, 375–393.

Ohkuma, T., Marukawa, H., Niihori, Y., & Kato, N. (1991). Full-scale measurement of wind pressures and response accelerations of a high-rise building. *Journal of Wind Engineering and Industrial Aerodynamics*, *38*(2–3), 185–196. https://doi.org/10.1016/0167-6105(91)90040-4

Roshko, A., & Lau, J. C. (1965). Some observations on the transition and reattachment of a free shear layer in incompressible flow. *Proceedings of the HeatTransfer and Fluid Mechanics Institute.*

Solari, G. (1993a). Gust buffeting. I: Peak wind velocity and equivalent pressure. *Journal of Structural Engineering*, *119*(2), 365–382.

Solari, G. (1993b). *Gust buffeting. II: dynamic alongwind response*. *119*(2), 383–398.

Solari, G, & Kareem, A. (1998). On the formulation of ASCE7-95 gust effect factor. *Journal of Wind Engineering and Industrial Aerodynamics*, *77–78*, 673–684. https://doi.org/10.1016/S0167-6105(98)00182-2

Standards Association of Australia (SAA). (1973). SAA loading code, Part 2: Wind forces. AS 1170.2-1973.

Surry, D., & Djakovich, D. (1995). Fluctuating pressures on models of tall buildings. *Journal of Wind Engineering and Industrial Aerodynamics*, *58*(1–2), 81–112. https://doi.org/10.1016/0167-6105(95)00015-J

Tanaka, H., Tamura, Y., Ohtake, K., Nakai, M., & Chul Kim, Y. (2012). Experimental investigation of aerodynamic forces and wind pressures acting on tall buildings with various unconventional configurations. *Journal of Wind Engineering and Industrial Aerodynamics*, *107*, 179–191. https://doi.org/10.1016/j.jweia.2012.04.014

Tieleman, H. W. (2003). Roughness estimation for wind-load simulation experiments. *Journal of Wind Engineering and Industrial Aerodynamics*, *91*, 1163–1173. https://doi.org/10.1016/S0167-6105(03)00058-8

Wu, C.-H., & Kopp, G. A. (2016). Estimation of Wind-Induced Pressures on a Low-Rise Building Using Quasi-Steady Theory. *Frontiers in Built Environment*, *2*, 1–15. https://doi.org/10.3389/fbuil.2016.00005

Wu, C. H. (2017). *Estimation of Turbulence Effects on Wind-Induced Suctions on the Roof of a Low-Rise Building*. Western University.

Zhou, Y., Kijewski, T., & Kareem, A. (2003). Aerodynamic Loads on Tall Buildings: Interactive Database. *Journal of Structural Engineering*, *129*(3), 394–404. https://doi.org/10.1061/(ASCE)0733-9445(2003)129:3(394)